

EPR identification of intrinsic defects in SiC

Feature Article

J. Isoya^{*,1}, T. Umeda¹, N. Mizuochi¹, N. T. Son², E. Janzén², and T. Ohshima³

¹ University of Tsukuba, Tsukuba 305-8550, Japan

² Department of Physics, Chemistry and Biology, Linköping University, 581 83 Linköping, Sweden

³ Japan Atomic Energy Agency, Takasaki 370-1292, Japan

Received 13 May 2008, accepted 19 May 2008

Published online 12 June 2008

PACS 61.72.jd, 61.72.up, 61.80.Fe, 76.30.Mi, 76.70.Dx

* Corresponding author: e-mail isoya@slis.tsukuba.ac.jp

The structure determination of intrinsic defects in 4H-SiC, 6H-SiC, and 3C-SiC by means of EPR is based on measuring the angular dependence of the ²⁹Si/¹³C hyperfine (HF) satellite lines, from which spin densities, sp-hybrid ratio, and p-orbital direction can be determined over major atoms comprising a defect. In most cases, not only the assignment of the variety due to the inequivalent sites (*h*- and *k*-sites in 4H-SiC) but also the identification of the defect species is accom-

plished through the comparison of the obtained HF parameters with those obtained from *first principles* calculations. Our works of identifying vacancy-related defects such as the monovacancies, divacancies, and antisite-vacancy pairs in 4H-SiC are reviewed. In addition, it is demonstrated that the observation of the central line of the T_{V2a} center of *S* = 3/2 has been achieved by pulsed-ELDOR.

© 2008 WILEY-VCH Verlag GmbH & Co. KGaA, Weinheim

1 Introduction Electron paramagnetic resonance (EPR) has been proved to be the most successful technique in identifying deep centers in silicon. The abundance of isotopes with non-zero nuclear spin (²⁹Si, *I* = 1/2, natural abundance 4.67%) is just right to keep the linewidth narrow enough for sufficient sensitivity and resolution and to observe the satellite lines due to hyperfine (HF) interactions easily. EPR has been also powerful in identifying point defects in diamond which supply smaller linewidth, although ¹³C (*I* = 1/2, 1.11%) enriched crystals were crucial for the identification in several cases [1–4]. As demonstrated typically by negatively charged vacancies [1, 5, 6] lattice relaxations involved in intrinsic defects are significantly different between silicon and diamond. The energy gap of SiC (*E_g* = 3.28 eV for 4H-SiC) is between that of silicon (*E_g* = 1.12 eV) and diamond (*E_g* = 5.47 eV). Thus, it is expected that the comparison of the same defect among silicon, diamond, and SiC should be useful for understanding the reconstruction of structure relaxations involved in intrinsic defects. Moreover, SiC is richer in the variety of intrinsic defects arising from two sublattices (Si and C), abundant polytypes (3C-, 4H-, and 6H-SiC), and the presence of defects specific in compound semiconduc-

tors such as antisites (Si_C, C_{Si}) and antisite-vacancy pairs. SiC is unique among compound semiconductors in having narrow EPR linewidths ($\Delta B_{pp} \sim 0.03$ mT) and non-zero nuclear spin isotopes with reasonable (²⁹Si, 4.7%) and tolerable (¹³C, 1.1%) natural abundance.

SiC is a promising semiconductor material for high-power, high-temperature, and radiation-tolerant devices. High-purity semi-insulating (SI) substrates are attained by utilizing intrinsic defects [7, 8]. To improve the efficiency of ion implantation doping, understanding the behavior of defects is critically important. The EPR spectrum of phosphorus-ion implanted 6H-SiC demonstrates the observation of residual defects after post-implantation annealing (Fig. 1).

In EPR spectra of intrinsic defects in SiC, several sets of ²⁹Si and/or ¹³C HF lines are expected to appear as satellite lines of strong primary lines. The angular dependence of the line positions of primary lines are described by the spin-Hamiltonian for an electron spin *S*,

$$\mathcal{H} = \beta_e \mathbf{S} \cdot \mathbf{g} \cdot \mathbf{B} + [\mathbf{S} \cdot \mathbf{D} \cdot \mathbf{S}] .$$

The first term represents the electron Zeeman interaction. The second term, representing the fine structure interaction,

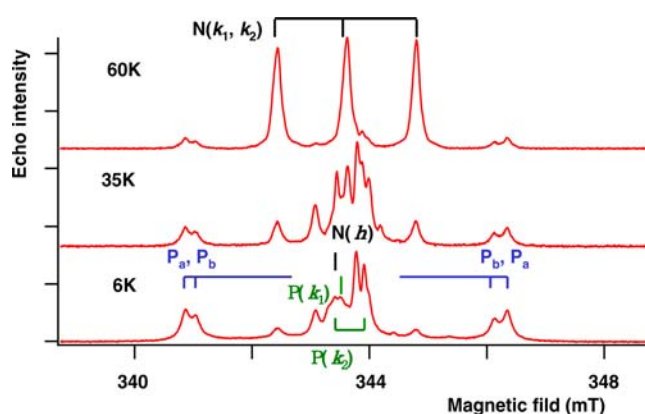


Figure 1 (online colour at: www.pss-b.com) Echo-detected EPR spectra of P-ion implanted 6H-SiC ($1 \times 10^{14} \text{ cm}^{-2}$ at each of 9 steps between 9 and 21 MeV at 800 °C, annealed at 1650 °C). Intensity of 2-pulse Hahn echo was measured as a function of the magnetic field strength. P_a , P_b which were originally observed in neutron-transmutation-doped 6H-SiC [9] are assigned by theoretical studies to be P donors at carbon sites [10]. At low temperatures, signals from centers with a long spin-lattice relaxation time are suppressed by using a fast repetition rate of the pulse sequence in accumulation. In addition to P and N donors (in the substrate), the signals from residual defects are noticed. The line positions of $P(k_1)$ and $P(k_2)$, which were originally observed in neutron-transmutation-doped 6H-SiC [11] and are assigned to the shallow P donors at silicon sites by using 6H-SiC doped during CVD growth [12], are indicated.

which splits the primary lines into $2S$ lines and splits the energy levels even at zero-magnetic field (zero-field splitting, ZFS), is included for a case with $S \geq 1$. Based on the g -values and hence the resonant line positions specific for each EPR center, different EPR spectra arising from different defects can be distinguished (Fig. 2).

The primary lines with high intensities are used to investigate how the concentration of defects varying upon different processing conditions, such as electron irradiation conditions (electron energy, dose and temperature), heat treatment, and light illumination. Before the microscopic structure is established, the EPR spectra are often tentatively referred by the labels such as Tn , Pn , Kyn , ($n = 1, 2, 3, \dots$) by using the initials of the research group, EIn , $HEIn$, $SiIn$ for those found in samples irradiated by electrons at room temperature or high temperatures and in SI samples, respectively, whereas IDn indicating intrinsic defects.

Although the g and D tensors are useful parameters for determination of the local symmetry and the spin multiplicity and hence the charge state, the primary lines lack definite chemical identity (Si or C). The detailed geometric and electronic structure identification comes from the HF interaction. For deep-level intrinsic defects in SiC, the wave function of the unpaired electron is extended to several atoms, Si_1 , Si_2 , ... and C_1 , C_2 , ... It is naturally expected that several major atoms comprising the defect such as four nearest-neighbors of vacancies and six nea-

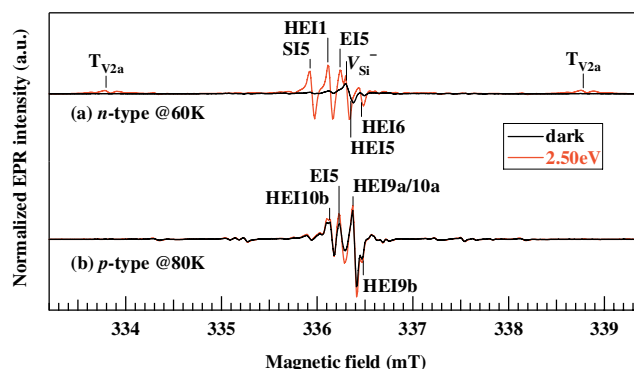


Figure 2 (online colour at: www.pss-b.com) Typical EPR and photo-EPR spectra of commercial 4H-SiC samples after electron irradiation. (a) n-type, $T_{\text{irr}} = 350 \text{ °C}$, $1 \times 10^{18} \text{ e/cm}^2$. (b) p-type, $T_{\text{irr}} = 800 \text{ °C}$, $2 \times 10^{18} \text{ e/cm}^2$. Electron irradiations were done at a constant energy of 3 MeV and temperature of T_{irr} (@JAEA Takasaki, Japan). These spectra were measured for $B \parallel [0001]$ using microwave of 9.4 GHz and 0.0002 mW, and magnetic-field modulation of 100 kHz and 0.05 mT. EPR signals in this figure are explained in the text.

rest-neighbors of divacancies should have a HF splitting large enough to be resolved from the primary lines. Since the natural abundance of ^{29}Si and ^{13}C is low and the number of major atoms of deep intrinsic defects is not large, each set of satellite lines arises from the case that one and only one of the major atoms is occupied by $^{29}\text{Si}/^{13}\text{C}$. The line positions of the i -th satellite lines are described by the spin-Hamiltonian

$$\mathcal{H} = \beta_e S \cdot g \cdot B + [S \cdot D \cdot S] + [S \cdot A_i \cdot I_i - g_{n,i} \beta_n I_i \cdot B],$$

where nuclear spin $I = 1/2$ for both ^{29}Si and ^{13}C and $g_n(^{29}\text{Si}) = -1.1106$, $g_n(^{13}\text{C}) = 1.40483$ [13]. The third and fourth terms represent the HF interaction with the nucleus of the i -th atom and the nuclear Zeeman interaction, respectively. For structure determination of intrinsic defects, the observation of $^{29}\text{Si}/^{13}\text{C}$ HF satellite lines from all of the major-component atoms of the defect is desired. Although the wave function of the unpaired electron extends to further atoms, their HF interactions are often too weak resulting in unresolvable HF structures which contribute only to the linewidth of the primary and satellite lines. The primary lines are usually arising from a combination that all of major-component atoms are occupied by isotopes with zero nuclear spin. The intensity ratio between the satellite lines and the primary lines is important to determine the chemical identity (which gives the HF interaction, ^{29}Si or ^{13}C) and the number of equivalent atoms.

Among major Si/C atoms of a defect, some are symmetry-related as in the case of three basal silicon atoms Si_{2-4} in the positively charged carbon vacancy ($S = 1/2$, C_{3v} symmetry at 150 K) in 4H-SiC (Fig. 3) [14]. For the magnetic field $B \parallel [0001]$, these three atoms are equivalent and their ^{29}Si satellite lines are superimposed as shown in Fig. 3. From the fit of the angular dependence of the line

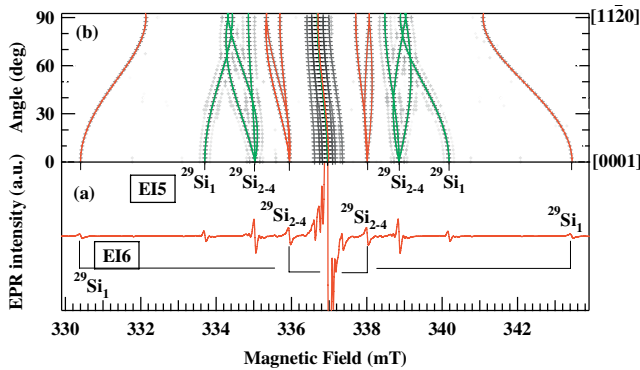


Figure 3 (online colour at: www.pss-b.com) (a) EPR spectrum of carbon vacancies (V_C) in p-type 4H-SiC (3 MeV electron irradiation at 800 °C with 2×10^{18} e/cm²) measured at 150 K. The E15 and E16 centers arise from V_C^+ at k - and h -sites, respectively [14]. Both centers exhibit four ^{29}Si HF satellite lines originating from four Si neighbors (Si_i and Si_{2-4}) of a V_C . (b) Angular dependence of line positions of ^{29}Si satellite lines, when magnetic field is rotating from [0001] to [1120]. (Umeda et al., Phys. Rev. B **69**, 121201(R) (2004). Copyright (2004) by the American Physical Society) [14].

positions of the satellite lines, usually obtained with \mathbf{B} rotating in high-symmetric planes such as (1 $\bar{1}$ 00) or (11 $\bar{2}$ 0), the HF tensor \mathbf{A}_i is determined. Upon rotation from [0001], the $^{29}\text{Si}_{2-4}$ HF lines split, and the symmetry of \mathbf{A}_{2-4} is determined to be C_{1h} from the pattern of roadmap of the HF lines. Here, the presence of ^{29}Si on one of three basal silicon atoms (Si_{2-4}) lowers the symmetry. We determine \mathbf{A}_i of one site (for example, Si_2). The line positions of the other symmetry-related sites (Si_3 and Si_4) are converted to those which should be obtained for the selected site (in this case, Si_2) by the rotation of the magnetic field in the other plane(s). Thus, \mathbf{A}_i with the symmetry lower than C_{3v} is also determined by a single rotation. \mathbf{A}_i of other sites symmetry-related to the selected site is obtained by symmetry operation. The pattern of the rotational plots shown in Fig. 3 is characteristic of the HF lines of the nearest-neighbors of monovacancy having C_{3v} symmetry.

The wave function of the unpaired electron is satisfactorily described by linear combination of atomic orbitals (LCAO)

$$\Psi = \sum_i \eta_i (\alpha_i \psi_{s,i} + \beta_i \psi_{p,i}),$$

where α_i and β_i ($\alpha_i^2 + \beta_i^2 = 1$) are the s- and p-orbital contributions of the i -th atom and the total spin density η_i^2 indicates the degree of the spin localization on the i -th atom. The HF tensor of the i -th atom \mathbf{A}_i has usually axial symmetry with the principal values $A_{\parallel}(i)$ and $A_{\perp}(i)$ or nearly uniaxial. The HF interaction is divided into isotropic part $A_{\text{iso},i}$ and anisotropic part b_i ,

$$A_{\text{iso},i} = [A_{\parallel}(i) + 2A_{\perp}(i)]/3 = \eta_i^2 \alpha_i^2 A_0,$$

$$b_i = [A_{\parallel}(i) - A_{\perp}(i)]/3 = \eta_i^2 \beta_i^2 b_0,$$

where we use $A_0 = 134.77$ mT, $b_0 = 3.83$ mT for ^{13}C and $A_0 = -163.93$ mT, $b_0 = -4.075$ mT for ^{29}Si [13]. In addition to the spin density η_i^2 and sp-hybrid ratio β_i^2/α_i^2 , the direction of the p_i -orbital is determined from the principal axes of \mathbf{A}_i . Thus, the observation of the HF structure, which gives the orbital parameters, is crucial for the structure identification of defects.

As typically demonstrated in the case of the neutral divacancy, $[V_{\text{Si}}V_{\text{C}}]^0$, in which the unpaired electrons are mostly localized on three nearest C neighbors of V_{Si} among the six nearest-neighbors [15], the wave function of unpaired electrons might extend quite unevenly among the major atoms comprising the intrinsic defects. In such a case, the identification of the defect from EPR data is not straightforward, since a part of the major atoms which do not give the $^{29}\text{Si}/^{13}\text{C}$ satellite lines are invisible in the EPR spectra. Now, the *first principles* calculations provide not only the predicted structure of intrinsic defects but also the expected HF parameters [16]. Thus, the comparison of HF parameters obtained by experiments and theoretical studies is often crucial for the defect identification (see Fig. 4).

For some of major-component atoms which exhibit a weak isotropic HF splitting with the anisotropy hidden underneath the linewidth, only the number of equivalent atoms and $\eta_i^2 \alpha_i^2$ are obtainable. Nevertheless, such information is still important in comparison with that obtained by theoretical studies. To extract the HF interactions hidden underneath the linewidth, we have applied pulsed ENDOR (electron nuclear double resonance) of pulsed EPR techniques which have much higher resolutions than that of the conventional EPR. The first-order ENDOR frequencies are determined as

$$h\nu_{\text{ENDOR}} = |M_S A_{\text{eff}} - g_n \beta_n B|$$

here h is the Planck constant, β_n the nuclear magneton and A_{eff} the effective HF splitting. Since the nucleus is unambiguously determined from the observed nuclear Zeeman frequency ($g_n \beta_n B/h$), ENDOR is useful for identifying the nucleus (^{29}Si or ^{13}C) giving rise to the resolved HF satellite

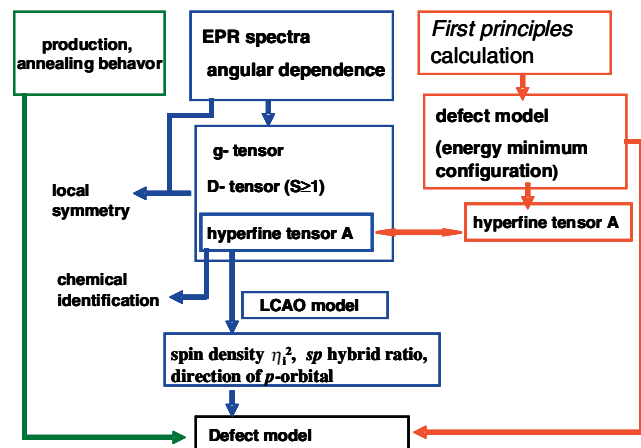


Figure 4 (online colour at: www.pss-b.com) Scheme of procedures of identification of intrinsic defects in SiC.

lines. Since the ENDOR frequencies depend on M_S ($\pm 1/2$ for $S = 1/2$, ± 1 and 0 for $S = 1$, $\pm 1/2$ and $\pm 3/2$ for $S = 3/2$), the spin multiplicity (S) can be determined. Actually, this technique was employed for the case of silicon vacancies (V_{Si}^- and T_{V2a} , $S = 3/2$) [17, 18].

The intensities of the $^{29}\text{Si}/^{13}\text{C}$ HF lines, which do lead to the decisive structure determination, are severely limited by their low natural abundances. To produce the defect of interest selectively at sufficient concentrations, we performed electron irradiation at various temperatures (-160°C to 800°C), with different doses (1×10^{17} – 1×10^{19} e/cm 2), and post-irradiation heat-treatment processes (100 – 1500°C) and used thick single-crystal samples (typically $3 \times 10 \times 1.5$ mm) of both n- and p-type of different dopant concentrations.

2 Isolated vacancy The lattice vacancy which is one of most fundamental intrinsic defects is also the primary defect produced upon irradiation with energetic particles. The mobility of isolated vacancy is remarkably different among diamond, SiC, and silicon. In SiC and diamond isolated vacancies are observable after electron irradiation at room temperature, at which divacancies and impurity-vacancy complexes are formed in silicon.

A variety of isolated vacancies arising from different sublattices (Si and C), inequivalent sites (hexagonal site h and cubic site k), and having different charge states is expected in 4H-SiC. The difference in the electron negativity (2.55 for C and 1.9 for Si on the Pauling scale) favors the negative charge state (-1) for the silicon vacancy (V_{Si}) and the positive charge state ($+1$) for the carbon vacancy (V_C). So far, several V_{Si}^- , V_C^+ and V_C^- centers have been identified by EPR in 3C-, 4H- and 6H-SiC.

First, let us consider the isolated vacancies in silicon. Features of the EPR spectra of V^+ (D_{2d} , $S = 1/2$) labeled Si-G1 and V^- (C_{2v} , $S = 1/2$) labeled Si-G2 [5, 6, 19] were successfully explained with a dominant Jahn–Teller distortion by using simple one-electron LCAO models illustrated in Fig. 5. Tetrahedral crystal field splits the defect molecular orbitals into a singlet a_1 and a triplet t_2 . In the positively charged vacancy (V^+), under undistorted T_d symmetry, two electrons enter into a_1 and the third electron enters into t_2 .

Thus, V^+ in silicon, which is subjected to a Jahn–Teller distortion, undergoes a tetragonal distortion and the resulting symmetry is D_{2d} (Fig. 5(b)). The orbital occupied by the unpaired electron (b_2) spreads equally over the four

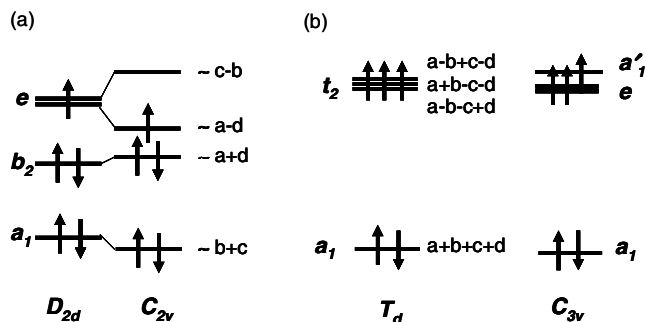


Figure 6 Energy levels of the negatively charged vacancy in a simple model of one-electron molecular orbital (a) for silicon and (b) for diamond and SiC. In C_{3v} symmetry, only a case with a singlet a'_1 higher than a doublet e is shown.

nearest-neighbors with the spin density $\eta^2 = 14.6\%$ and the sp-hybrid ratio $\beta^2/\alpha^2 = 5.5$ on each silicon. In the $\langle 100 \rangle$ axial symmetry, the two atoms in two pairs (b, c and a, d) are pulled together [19].

Since the b_2 orbital can accommodate one more electron, the neutral vacancy with four electrons has D_{2d} symmetry and $S = 0$. Under D_{2d} symmetry, the fifth electron of the negatively charged vacancy (V^-) goes into a degenerate e level. Thus, further Jahn–Teller distortion lowers the symmetry to C_{2v} , resulting in the effective spin $S = 1/2$ (Fig. 6(a)). The distortion is pulling one pair of atoms (b and c) together toward each other and separating the other pair of atoms (a and d) slightly. The unpaired electron is localized mainly on two (a and d) of the four nearest-neighbors with the spin density $\eta^2 = 27.3\%$ and the sp-hybrid ratio $\beta^2/\alpha^2 = 2.52$ [5, 6]. In both V^+ and V^- , the sum of the spin densities of the nearest-neighbors is similar between V^+ (58.4%) and V^- (54.6%).

V^- in diamond has T_d symmetry with the effective spin $S = 3/2$ (three electrons in the triply degenerate t_2 level) as shown in Fig. 6(b) left. The orbitally nondegenerate 4A_2 state is not subjected to a Jahn–Teller distortion. The large fraction ($\sim 83\%$) of the unpaired electron is localized on the four nearest-neighbors [1]. The electron–electron repulsion due to the strong localization favors the high spin state in which three electrons occupy three different orbitals. In silicon, the energy gain is obtained by Jahn–Teller distortion, while the electron–electron repulsion is lowered by a large delocalization. The extent of the wave function of the unpaired electron was confirmed by ENDOR measure-

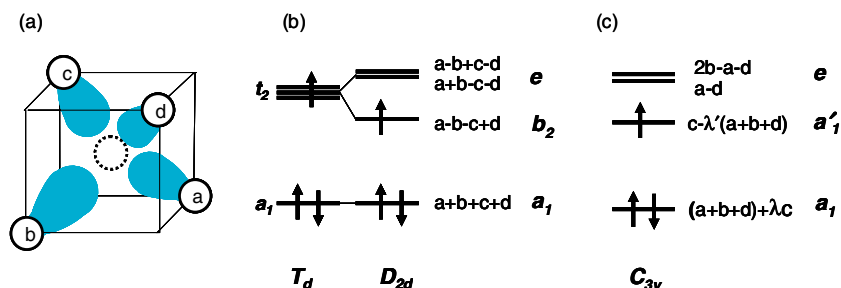


Figure 5 (online colour at: www.pss-b.com) Energy levels of the positively charged vacancy in a simple model of one-electron molecular orbital constructed by the four dangling bonds shown in (a). Under T_d symmetry, both tetragonal and trigonal distortions would remove the degeneracy. Under C_{3v} symmetry, further distortion is required if a doublet e is lower than a'_1 .

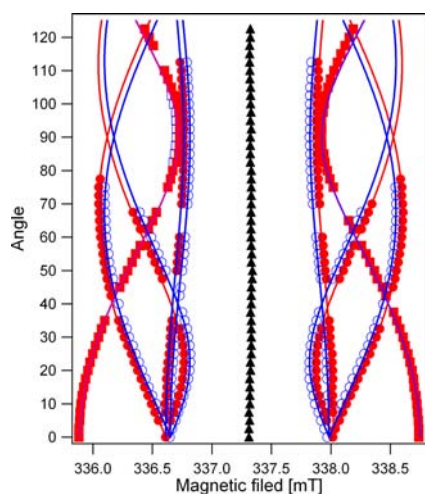


Figure 7 (online colour at: www.pss-b.com) Observation of two types (open and solid symbols) of V_{Si}^- in 4H-SiC measured by cw-EPR at room temperature (B in the $(1\bar{1}00)$ plane, 0° for $B||[0001]$ and 90° for $B||[11\bar{2}0]$). Open circles and squares from $V_{Si}^-(h)$ and filled circles and squares from $V_{Si}^-(k)$. (Mizuochi et al., Phys. Rev. B **68**, 165206 (2003). Copyright (2003) by the American Physical Society) [22].

ments up to the 17-th atom along the $\langle 110 \rangle$ zigzag chain [6]. Thus, important factors which govern the geometric and the electronic structures are the degree of structure relaxation and the electron–electron repulsion.

2.1 Silicon vacancy in SiC In SiC, negatively charged silicon vacancies (V_{Si}^-) are found in 3C-, 4H-, and 6H-SiC [17, 18, 22]. Basically, they are similar to V^- in diamond in taking the ground state of high spin state ($S = 3/2$). The T_d symmetry of V_{Si}^- in 3C-SiC (the T1 center) was confirmed by the angular dependence of ^{13}C HF lines of the nearest-neighbors [20, 21]. In the T_d symmetry, all three $\Delta M_S = \pm 1$ transitions of $S = 3/2$ are superimposed since the ZFS vanishes. The effective spin $S = 3/2$ of V_{Si}^- in 4H-SiC was confirmed by the ENDOR measurements [17]. This high spin state has been ascribed to predominant tetrahedral character of the local structure which is indicated by isotropic g -value, isotropic ^{29}Si HF interactions of next-nearest-neighbors, and the absence of ZFS. By measuring the angular dependence of ^{13}C HF lines of the nearest-neighbors, two spectra labeled $V_{Si}^-(I)$ and $V_{Si}^-(II)$ are distinguished (Fig. 7) [22]. It is emphasized that the V_{Si}^- centers are very similar between 6H-SiC and 4H-SiC (Figs. 8(a) and (b)). From the intensity ratio of the corresponding spectra in 6H-SiC, $V_{Si}^-(I)$ and $V_{Si}^-(II)$ are assigned to be arising from $V_{Si}^-(h)$ and $V_{Si}^-(k)$, respectively. In both types, the C_{3v} symmetry is demonstrated by the inequivalence in η_i^2 and β_i^2/α_i^2 between C_1 and C_{2-4} (Table 1, Fig. 9). Thus, the arrangement of nearest-neighbors of V_{Si}^- in 4H-SiC is slightly distorted from regular tetrahedron.

The T_{V2a} center can be observed by photoluminescence (PL), which is called the V2 line (1.352 eV). The correspondence between T_{V2a} and V2 was demonstrated by optically detected magnetic resonance (ODMR) [23]. The T_{V2a}

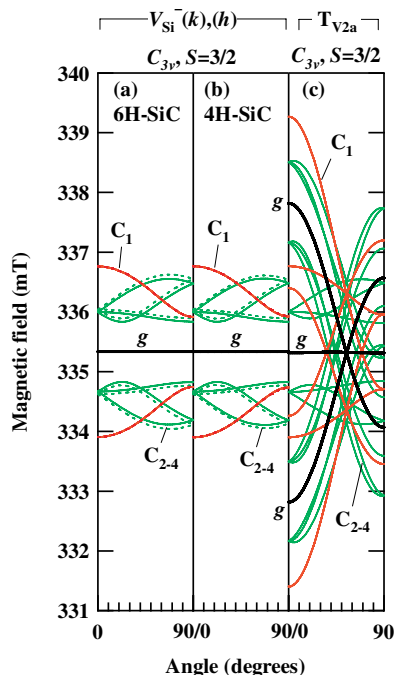


Figure 8 (online colour at: www.pss-b.com) Angular maps for silicon vacancy centers in 6H- and 4H-SiC. (a) V_{Si}^- centers in 6H-SiC [22]. (b) V_{Si}^- centers in 4H-SiC [22]. Solid and dashed curves correspond to type (I) and (II), respectively. (c) T_{V2a} center in 4H-SiC (V_{Si}^- with non-zero ZFS) [24]. These maps were simulated on our web site “EPR in Semiconductors” (<http://www.kc.tsukuba.ac.jp/div-media/epr/>) using a microwave frequency of 9.400 GHz and B rotation from $[0001]$ to $[11\bar{2}0]$ (from 0° to 90°). Primary and ^{13}C HF satellite lines are denoted by “g” and “ C_{1-4} ” (thick and thin lines), respectively, where C_1 means a c -axial neighbor of V_{Si}^- and C_{2-4} means other three neighbors (see Fig. 9). Only main HF lines are shown here.

center which does exhibit ZFS ($|D| = 35.1$ MHz) [23] has been identified as a family of V_{Si}^- having $S = 3/2$ [18, 24]. Similar to the V_{Si}^- center, the EPR spectra of T_{V2a} center have ^{29}Si satellites arising from twelve equivalent Si atoms in the next-nearest-neighbor-shell of V_{Si}^- , which are drawn

Table 1 Orbital parameters of $V_{Si}^-(h)$, $V_{Si}^-(k)$ and T_{V2a} in 4H-SiC obtained from the ^{13}C HF tensors of the carbon nearest-neighbors (C_{1-4}): the spin density η_i^2 , the sp-hybrid ratio β_i^2/α_i^2 , and the angle θ between the p-orbital and the c -axis (see Fig. 9). “total” means the sum of η_i^2 for C_{1-4} atoms.

center, symmetry	atom	η_i^2 (%)	β_i^2/α_i^2	θ
$V_{Si}^-(h)$ (C_{3v})	C_1	15.9	11.3	0°
	C_{2-4}	16.1	12.7	110.0°
	total	64.2		
$V_{Si}^-(k)$ (C_{3v})	C_1	15.9	11.2	0°
	C_{2-4}	16.2	11.9	109.2°
	total	64.5		
T_{V2a} (C_{3v})	C_1	15.4	10.7	0°
	C_{2-4}	15.6	12.2	107.5°
	total	62.2		

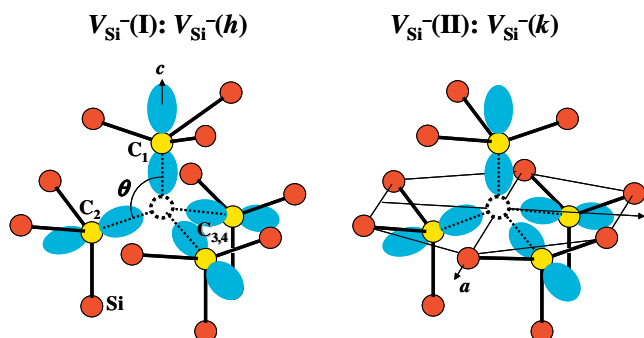


Figure 9 (online colour at: www.pss-b.com) Atomic structures of silicon vacancy centers $V_{\text{Si}}^-(h)$ and $V_{\text{Si}}^-(k)$ in 4H-SiC. The sp-hybridized orbitals of the defects are schematically drawn in the figure.

in Fig. 9. In both V_{Si}^- and T_{V2a} , the ^{29}Si HF splitting is isotropic within the resolution of cw-EPR and the satellite lines arising from two ^{29}Si nuclei on among these twelve silicon atoms are also observed. The angular dependence of three primary lines and the ^{13}C satellites of four nearest-neighbors (C_{1-4}) is shown in Fig. 8(c). The complete analysis of the T_{V2a} spectrum was achieved by utilizing the enhancement of the signal intensity due to electron spin polarization by light illumination [24, 25]. However, the central primary line of T_{V2a} was often missing, because it was not enhanced by illumination and was usually hidden underneath the V_{Si}^- signal. This misled to that T_{V2a} originates from V_{Si}^0 with $S = 1$ [25]. The observation of the central primary line can be achieved by a pulsed-ELDOR technique shown in Section 3. The spin multiplicity of T_{V2a} has been determined to be $S = 3/2$ by the nutation method of pulsed-EPR [24] and by pulsed ENDOR [18]. The C_{3v} symmetry of T_{V2a} , which was already manifested by the ZFS, has been supported by the larger deviation from a regular tetrahedral angle ($109.5^\circ \rightarrow 107.5^\circ$, see Table 1).

The defect wave function is rather delocalized for V_{Si}^- in SiC (62–65% on C_{1-4} atoms, see Table 1) than for V^- in diamond (83%). The sp-hybrid ratio is larger than that (~ 7) of V^- in diamond. Four carbon dangling bonds of V_{Si}^- are well separated in SiC [26, 27], preserving the high spin state of V_{Si}^- . This situation is strikingly contrast to the case of carbon vacancies explained in the next section.

2.2 Carbon vacancy in SiC Positively charged carbon vacancies (V_{C}^+ , $S = 1/2$) have been found in 4H- and 6H-SiC but not in 3C-SiC. In 4H-SiC, a negatively charged carbon vacancy (V_{C}^- , $S = 1/2$) was also found.

The EI5 [28] and EI6 [29] centers in 4H-SiC have been established to be V_{C}^+ at cubic (k) and hexagonal (h) sites, respectively [14, 30]. Similarly, the $\text{Ky}1/2$ and $\text{Ky}3$ centers in 6H-SiC have been identified as V_{C}^+ at two cubic (k_1 , k_2) and one hexagonal sites, respectively [31]. All of these spectra exhibit ^{29}Si HF satellite lines arising from four Si neighbors of a V_{C} . Angular dependences of the primary and ^{29}Si HF lines are summarized in Fig. 10(a) to (d).

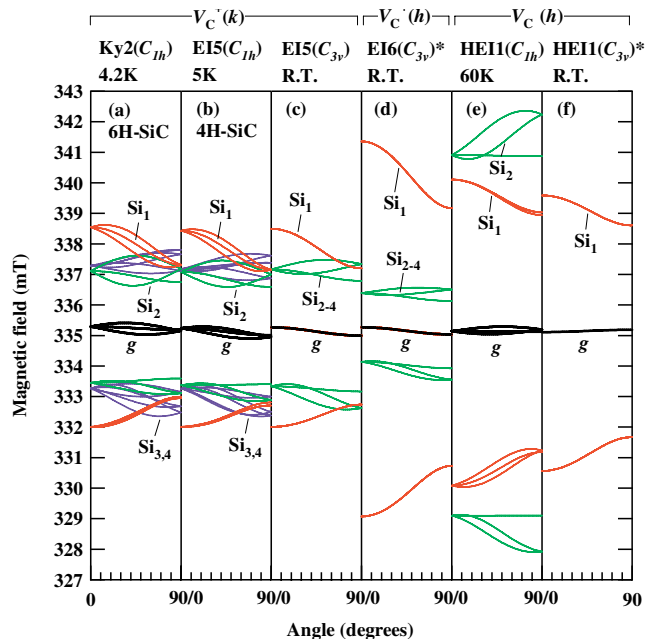


Figure 10 (online colour at: www.pss-b.com) Angular maps for carbon vacancy centers in 6H- and 4H-SiC. (a) $\text{Ky}2$ center or V_{C}^+ at a cubic site in 6H-SiC [31]. (b)–(c) EI5 center or $V_{\text{C}}^+(k)$ in 4H-SiC [14, 30]. (d)–(e) EI6 center or $V_{\text{C}}^+(h)$ in 4H-SiC [14]. (e)–(f) HEI1 center or $V_{\text{C}}^+(h)$ in 4H-SiC [32]. These maps were simulated on “EPR in Semiconductors” (<http://www.kc.tsukuba.ac.jp/div-media/epr/>) using a microwave frequency of 9.400 GHz and \mathbf{B} rotation from $[0001]$ to $[11\bar{2}0]$ (from 0° to 90°). Primary and ^{29}Si HF lines are denoted by “g” and “ Si_{1-4} ”, respectively, where Si_1 means a c -axial neighbor of V_{C} and Si_{2-4} means other three neighbors (see Fig. 11). Only main HF lines are shown here. * EPR parameters are gradually changed as a function of temperature.

Again we can find a close similarity between the EPR spectra in 6H-SiC (Fig. 10(a)) and 4H-SiC (Fig. 10(b)).

The V_{C}^+ centers are typical examples in which the structure relaxation is remarkably different between the inequivalent sites (Fig. 11) and the assignment of EPR spectra has been achieved by agreement between the observed

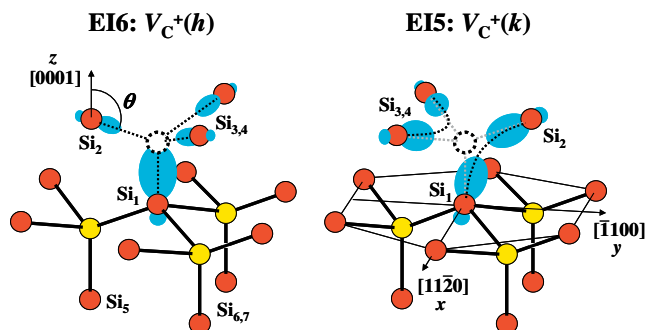


Figure 11 (online colour at: www.pss-b.com) Atomic structures of carbon vacancy centers $V_{\text{C}}^+(h)$ and $V_{\text{C}}^+(k)$ in 4H-SiC. The sp-hybridized orbitals of the defects are schematically shown in the figure.

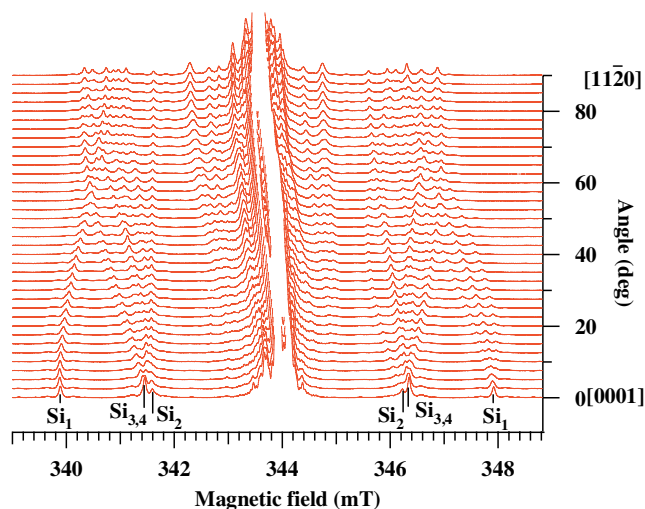


Figure 12 (online colour at: www.pss-b.com) Angular-dependence measurement on ^{29}Si HF lines of $V_C^+(k)$ with C_{1h} symmetry at 5 K. These spectra were measured using 2-pulse Hahn echo ($\pi/2$ pulse – τ – π pulse – τ – echo, $\tau = 1.2 \mu\text{s}$, repetition time = 10 ms) of pulsed EPR.

^{29}Si HF tensors and those obtained by the *first principles* calculations [16, 30]. As shown in Table 2, the HF parameters obtained from the *first principles* calculation are consistent with those from EPR measurements at low temperatures. We owe to the contributions of theoretical groups that two EPR spectra EI5/EI6 significantly different in the symmetry and the spin distribution among four-nearest-neighbors are assigned to $V_C^+(k)/V_C^+(h)$ [16, 30].

In 4H-SiC, for both $C(h)$ and $C(k)$ sites, there are two magnetically distinguishable orientations of $[\text{CSi}_4]$ tetrahedron, $[\text{Si}_1\text{C}(h/k)\text{Si}_2\text{Si}_3\text{Si}_4]$ and $[\text{Si}_1\text{C}(h'/k')\text{Si}_2\text{Si}_3\text{Si}_4]$. In analyzing the angular dependence of the ^{29}Si HF lines of V_C^+ , the presence of two orientations needs to be considered. However, instead of going into these technical details, we discuss the structure relaxation by using one tetrahedron composed of the nearest-neighbors $[\text{Si}_1(\text{Si}_2\text{Si}_3\text{Si}_4)]$,

where Si_1 is the unique silicon atom located on the $[0001]$ direction.

An example of the angular-dependence measurement is shown in Fig. 12 for the EI5 center at 5 K. The angular dependence for this center ($V_C^+(k)$) is classified into two phases: one is observed below 50 K (C_{1h} symmetry, Fig. 10(b)), and another is seen above 50 K (C_{3v} symmetry, Fig. 10(c)) [30]. As the effect of lowering the local symmetry from C_{3v} to C_{1h} , in the first place, Si_2 is not symmetry related to $\text{Si}_{3,4}$ where Si_3 and Si_4 are mirror-symmetric with respect to the $(11\bar{2}0)$ plane (Fig. 11). As a result, with $\mathbf{B} \parallel [0001]$, three sets of ^{29}Si HF lines, Si_1 , Si_2 and $\text{Si}_{3,4}$ are observed as is seen in Fig. 12, while $\text{Si}_{2,4}$ become equivalent for $\mathbf{B} \parallel [0001]$ under C_{3v} symmetry (Fig. 3). In the second place, the number (orientational degeneracy) of symmetry-related sites, which have an identical structure except orientations in the lattice, is increased. Upon rotation with $\mathbf{B} \perp [1100]$, the primary line and the set of ^{29}Si , the set of Si_2 split into three lines. The set of $\text{Si}_{3,4}$ splits into six lines. These behaviors are shown in Fig. 10(b).

From the obtained HF parameters (Table 2), the spin density (η^2), sp-hybrid ratio (β^2/α^2), and the direction of p-orbital [polar angles of θ or (θ, ϕ)] of nearest-neighbor silicon atoms are estimated (Table 3). As is drawn in Fig. 11, the p-orbital directions of Si_1 and Si_2 indicate that two dangling bonds of Si_1 and Si_2 are tilted to approach each other to form a $\text{Si}_1\text{--Si}_2$ bond. A similar reconstructed bond between Si_3 and Si_4 is formed by tilting of Si_3 and Si_4 dangling bonds.

At high temperatures, rapid thermally-activated reorientations (bond switching $[\text{Si}_1\text{--Si}_2, \text{Si}_3\text{--Si}_4] \leftrightarrow [\text{Si}_1\text{--Si}_3, \text{Si}_4\text{--Si}_2] \leftrightarrow [\text{Si}_1\text{--Si}_4, \text{Si}_2\text{--Si}_3]$) results in C_{3v} symmetry. Features characteristic to reorientation effects, such as the lifetime broadening of the low-temperature spectrum and the motional narrowing of the high-temperature spectrum were observed as a function of temperature. From the analysis of the reorientation time, the activation energy of the reorientation was estimated to be 0.015 eV [30].

Table 2 Principal values (in unit of mT) and directions of ^{29}Si HF tensors of carbon vacancy centers in 4H-SiC. θ or (θ, ϕ) represents the principal axis of A_{zz} with respect to the Cartesian coordinate defined in Fig. 11.

center symmetry	atom	first-principles calculation				experiment (EPR, 5K)				Ref.
		A_{xx}	A_{yy}	A_{zz}	θ or (θ, ϕ)	A_{xx}	A_{yy}	A_{zz}	θ or (θ, ϕ)	
$V_C^+(k)$ (C_{1h})	Si_1	4.17	4.11	6.13	(5.4°, 90°)	4.44	4.36	6.46	(7.7°, 90°)	[30]
	Si_2	3.74	3.69	5.44	(117.0°, 270°)	3.25	3.19	4.74	(121.5°, 270°)	
	$\text{Si}_{3,4}$	3.80	3.75	5.51	(105.7°, 61°) (105.7°, 119°)	3.85	3.81	5.52	(103.2°, 67.4°) (103.2°, 112.6°)	
$V_C^+(h)$ (C_{3v})	Si_1	9.89	9.89	15.27	0°	10.61	10.61	15.48	0°	[30]
	$\text{Si}_{2,4}$	0.59	0.59	1.21	98.8°	1.40	1.40	2.11	97.7°	
	$\text{Si}_{5,7}$	0.92	0.92	1.17	−18.2°	0.70	0.70	0.87	−15.5°	
$V_C^-(h)$ (C_{1h})	Si_1	7.78	7.78	10.03	(7°, 270°)	7.76	7.76	10.07	(7.1°, 270°)	[32]
	Si_2	11.24	11.24	14.45	(101°, 270°)	11.78	11.67	15.19	(101.2°, 270°)	

Table 3 Orbital parameters of V_C^+ and V_C^- in 4H-SiC obtained from the ^{29}Si HF tensors of the nearest-neighbors (Si_{1-4}) of V_C : The spin density η_i^2 , the sp-hybrid ratio β_i^2/α_i^2 , and the direction of the p-orbital θ or (θ, ϕ) with respect to the Cartesian coordinate defined in Fig. 11.

center, symmetry	atom	η_i^2 (%)	β_i^2/α_i^2	θ or (θ, ϕ)
$V_C^+(k)$ 150 K (C_{3v})	Si_1	19.6	5.3	0°
	Si_{2-4}	15.1	5.0	109.2°
	total	64.9		
	5K (C_{1h})	Si_1	19.9	5.4 ($7.7^\circ, 90^\circ$)
		Si_2	14.7	5.4 ($121.5^\circ, 270^\circ$)
		$\text{Si}_{3,4}$	16.5	5.1 ($103.2^\circ, 67.4^\circ$) ($103.2^\circ, 112.6^\circ$)
	total	67.6		
$V_C^+(h)$ 150 K (C_{3v})	Si_1	33.4	5.3	0°
	Si_{2-4}	9.3	5.5	102.6°
	total	61.3		
	5K (C_{3v})	Si_1	47.3	5.3 0°
		Si_{2-4}	6.9	5.9 97.7°
	total	68.0		
$V_C^-(h)$ 60 K (C_{1h})	Si_1	24.1	3.6	$(7.1^\circ, 270^\circ)$
	Si_2	36.6	3.6	$(101.2^\circ, 270^\circ)$
	total	60.7		

On the other hand, $V_C^+(h)$ (the EI6 center) keeps C_{3v} symmetry at 5 K [14], although the *first principles* calculation predicted a possible configuration having C_{1h} symmetry [16]. As is seen in Fig. 10(d), ^{29}Si HF splittings are much larger for Si_1 than other three Si neighbors (Si_{2-4}) of a V_C , indicating a strong localization on the Si_1 atom ($\eta^2 = 33.4\text{--}47.3\%$, see Table 3). The displacement of Si_1 along the [0001] direction away from Si_{2-4} is the major part of the structure relaxation. Due to the strong spin localization on Si_1 , ^{29}Si HF interaction from Si_{5-7} atoms behind Si_1 (see Fig. 11) can be also observed. Using a pulsed ENDOR technique, the anisotropy of the Si_{5-7} HF lines was resolved as shown in Fig. 13. The EI6 EPR spectrum is strongly temperature dependent. As temperature increases, the spin distribution on Si_1 is shifted to Si_{2-4} (Table 3). Accordingly, with $\mathbf{B} \parallel [0001]$, the ^{29}Si HF splitting decreases for Si_1 and Si_{5-7} , and increases for Si_{2-4} . At a low temperature limit, the sum of η^2 of four nearest-neighbors is the same for $V_C^+(h)$ and $V_C^+(k)$ (68.0% and 67.6%, respectively), exhibiting a stronger localization than the case of V^+ in silicon (58.5%).

In 4H-SiC, a negatively charged carbon vacancy can be also observed (Fig. 2(a)), which was named the HEI1 center ($S = 1/2$) [32]. Two angular maps of this center are shown in Figs. 10(e) and (f). Depending on temperature, the HEI1 EPR spectrum exhibits C_{1h} and C_{3v} symmetries, as similarly to $V_C(k)$. The transition temperature is about 70 K. In the C_{1h} configuration (< 70 K), the unpaired electron is mainly localized on two Si neighbors (Si_1 and one of Si_{2-4}) of V_C . This is just the same trend as observed for V^- in silicon [5, 6]. As a result, two sets of ^{29}Si HF lines are clearly appeared (Fig. 10(e)). The structure relaxation takes

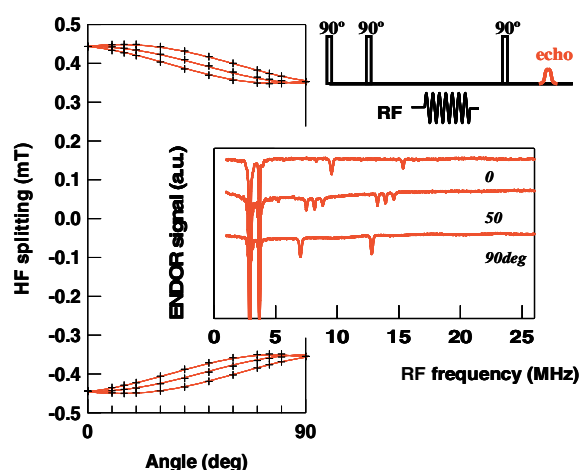


Figure 13 (online colour at: www.pss-b.com) Angular dependence of ^{29}Si ENDOR frequencies of Si_{5-7} (10 K). The small anisotropy is resolved by pulsed ENDOR. (Umeda et al., Phys. Rev. B 69, 121201(R) (2004). Copyright (2004) by the American Physical Society) [14].

place as to form a $\text{Si}_1\text{--Si}_2$ (or $\text{Si}_1\text{--Si}_3$ or $\text{Si}_1\text{--Si}_4$) pair. Likewise the case of $V_C^+(k)$, thermally activated reorientation results in C_{3v} symmetry at high temperatures. Furthermore, the $^{29}\text{Si}_2$ satellite line disappears due to the lifetime broadening (Fig. 10(f)). From the lifetime analysis, the reorientation activation energy was estimated to be 0.020 eV, which is slightly larger than that for $V_C^+(k)$. The sum of η^2 of the two nearest-neighbors is 60.7%, which is larger again than the case of silicon (55.8%). Comparing with the theoretical \mathbf{A} tensors, this V_C^- center is assigned to $V_C^-(h)$ (Table 2) [32]. The *first principles* calculation predicted that the $V_C^-(k)$ center is distinguishable due to its different HF signature, however, the corresponding EPR signal has not been identified.

3 Pulsed ELDOR of T_{V2a} : Observation of missing central line The EPR spectrum of T_{V2a} ($S = 3/2$, $|D| = 35.1$ MHz) is expected to be composed of three lines arising from three $\Delta M_S = \pm 1$ transitions, $+3/2 \leftrightarrow +1/2$, $+1/2 \leftrightarrow -1/2$, $-1/2 \leftrightarrow -3/2$. The echo-detected EPR spectrum (130 K, $\mathbf{B} \parallel [0001]$) of n-type 4H-SiC irradiated by electrons (3 MeV, 4×10^{18} e/cm 2) at room temperature is shown in Fig. 14. In dark (Fig. 14(b)), the central line of T_{V2a} ($+1/2 \leftrightarrow -1/2$ transition) is hidden underneath the strong signal of V_{Si}^- ($S = 3/2$, $D \sim 0$) due to lower concentrations. Under illumination of laser light (808 nm), the intensity of the two outer lines of T_{V2a} is strongly enhanced by electron spin polarization to surpass that of V_{Si}^- as shown in Fig. 14(a). However, the $+1/2 \leftrightarrow -1/2$ transition is not enhanced by illumination. Thus, the central line corresponding to the $+1/2 \leftrightarrow -1/2$ transition of T_{V2a} has not been revealed [23–25, 33].

The polarization under illumination is explainable by selective population onto two levels, either $\pm 1/2$ ($D > 0$) or $\pm 3/2$ ($D < 0$), among four M_S levels of $S = 3/2$. Here,

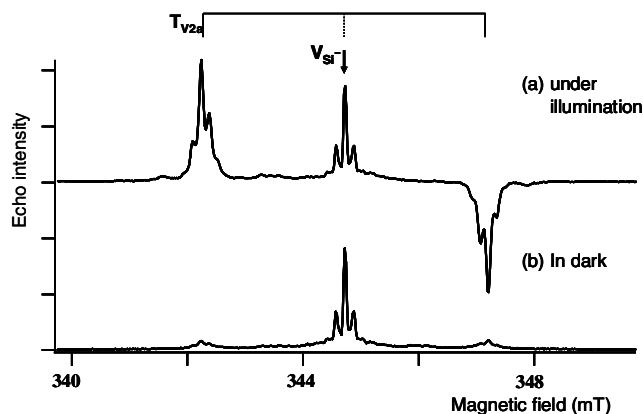


Figure 14 Echo-detected EPR spectra of electron irradiated n-type 4H-SiC (130 K, $B \parallel [0001]$). The intensity of 2-pulse Hahn echo is plotted against the magnetic field strength. Here, the positive peaks correspond to the absorption.

we assume that the $\pm 1/2$ levels should be selectively populated and $D > 0$. Then, the low-field line exhibiting strongly enhanced absorption is assigned to the $+3/2 \leftrightarrow +1/2$ transition (higher level is much less populated, $p(+3/2) \ll p(+1/2)$) and the high-field line exhibiting strong emission (the higher level has much larger population, $p(-1/2) \gg p(-3/2)$) is assigned to the $-1/2 \leftrightarrow -3/2$ transition. Here, $p(M_S)$ denote the population of the M_S level.

Since the microwave-induced transition probability is the same for both of the $\Delta M_S = \pm 1$ transitions (upward and downward transitions), the EPR signal intensity is proportional not only to the concentration of the defect but also to the population difference of the two M_S levels involved in the transition. The strong signal enhancement indicates that the absolute values of the population difference $|p(+3/2) - p(+1/2)|$ and $|p(-1/2) - p(-3/2)|$ is much larger than those in thermal equilibrium. No appearance of the $+1/2 \leftrightarrow -1/2$ transition of $T_{V_{2a}}$ indicates that no extra population difference is created under illumination. For

simplicity, we assume that the $\pm 1/2$ levels are equally populated under illumination ($p(+1/2) \sim p(-1/2)$).

If the large population difference between the $-1/2$ and $-3/2$ levels (or between the $+3/2$ and $+1/2$ levels) attained by illumination should be created also for between the $+1/2$ and $-1/2$ levels, as inferred from Fig. 14, the intensity of the $+1/2 \leftrightarrow -1/2$ transition of $T_{V_{2a}}$ can exceed that of the strong V_{Si}^{-} signal. We have tried to transfer the polarization of the $+3/2 \leftrightarrow +1/2$ transition ($-1/2 \leftrightarrow -3/2$ transition) to the $+1/2 \leftrightarrow -1/2$ transition by using 180° pulse of the $+3/2 \leftrightarrow +1/2$ ($-1/2 \leftrightarrow -3/2$) transition. Here, the 180° pulse is used to swap the populations of the levels between which the transition is induced. Then, we need a microwave pulse with frequencies different from the one used for observing the signal of the $+1/2 \leftrightarrow -1/2$ transition (Fig. 15). We have carried out pulsed ELDOR (electron–electron double resonance) experiments at 130 K under illumination of laser light (808 nm).

In the first place, the frequency-swept ELDOR experiments were carried out with the magnetic field fixed at the central signal (Fig. 16). For observing the signal of the $+1/2 \leftrightarrow -1/2$ transition of $T_{V_{2a}}$ which is expected to appear overlapped with that of V_{Si}^{-} , a pulse sequence of 3-pulse inversion recovery, ($180^\circ - t_0 - 90^\circ - \tau - 180^\circ - \tau - \text{echo}$, where $t_0 = 4 \mu\text{s}$ and $\tau = 1 \mu\text{s}$ are fixed), was employed, here, t_0 is sufficiently shorter than the spin–lattice relaxation time. Hahn-echo ($90^\circ - \tau - 180^\circ - \tau - \text{echo}$) generated by the second and the third pulses, which has usually a role to make the z component of the magnetization M_z at time t_0 observable, is used to measure the polarization of the $+1/2 \leftrightarrow -1/2$ transition of $T_{V_{2a}}$ induced by the ELDOR pulse. When no ELDOR pulse is applied, the signal corresponding to the inversion of the V_{Si}^{-} signal was observed. The 180° pulse (duration 80 ns) at $t = 0$ inverts the population difference of V_{Si}^{-} , however does not alter the zero-intensity of the $+1/2 \leftrightarrow -1/2$ transition of $T_{V_{2a}}$ since $p(+1/2) \sim p(-1/2)$. Thus, the baseline in Fig. 16 corresponds to the echo height of the inverted V_{Si}^{-} signal.

The ELDOR pulse, of which duration (116 ns) was chosen to attain the flipping angle of $\sim 180^\circ$, was applied at

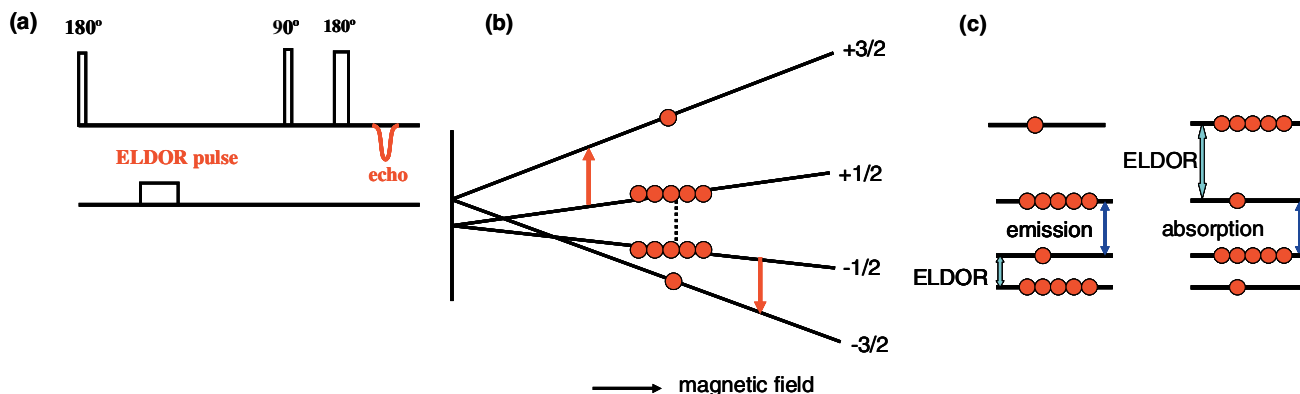


Figure 15 (online colour at: www.pss-b.com) (a) Pulsed-ELDOR experiment, (b) population under illumination without ELDOR pulse ($D > 0$ and selective population onto $\pm 1/2$ levels are assumed), (c) population after ELDOR pulse.

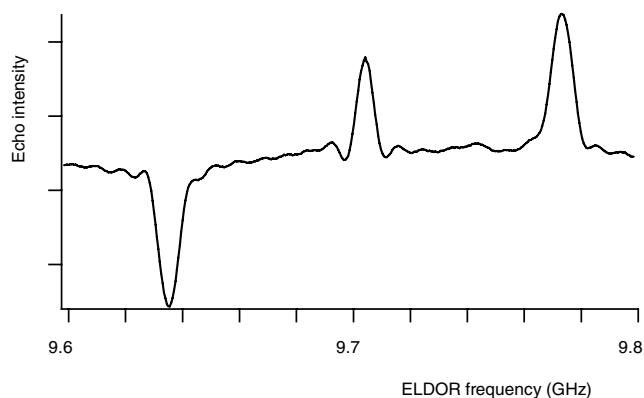


Figure 16 Frequency-swept pulsed-ELDOR spectrum (130 K, $B \parallel [0001]$). The intensity of 3-pulse inversion recovery of the central signal (9.705 GHz) was monitored as a function of the microwave frequency of the ELDOR pulse.

$t = 1 \mu\text{s}$. The frequency (9.705 GHz) of the 3-pulse inversion recovery sequence as well as the coherent detection is tuned to that of the resonator loaded with the sample. The resonator has a large bandwidth due to low- Q which is inherent to pulse experiments for achieving a short deadtime. When the frequency of the ELDOR pulse was varied (Fig. 16), the echo height is significantly affected at 9.635 GHz and at 9.775 GHz as well as at 9.705 GHz. The change brought at 9.705 GHz is caused by the flipping of the central signal mainly due to V_{Si}^- . The signal of the $+1/2 \leftrightarrow -1/2$ transition of T_{V2a} , which is also resonant to 9.705 GHz, was not affected by the flipping by the ELDOR pulse of 9.705 GHz since $p(+1/2) \sim p(-1/2)$. Two frequencies, 9.635 GHz and 9.775 GHz correspond to the $-1/2 \leftrightarrow -3/2$ and $+3/2 \leftrightarrow +1/2$ transitions of T_{V2} , respectively, at the magnetic field of the central signal (Fig. 15(c)). We note that these frequencies are $\sim 9.705 \text{ GHz} \pm 2|D|$. The change of the echo intensity brought by the ELDOR pulse of these frequencies, stimulated emission at 9.635 GHz and stimulated absorption

at 9.775 GHz, is ascribed to the appearance of the strong signal from the $+1/2 \leftrightarrow -1/2$ transition of T_{V2a} .

In the second place, the field-swept ELDOR experiments were carried out to obtain the spectral features of the $+1/2 \leftrightarrow -1/2$ transition of T_{V2a} . We have three signals, the signal of $+3/2 \leftrightarrow +1/2$ of T_{V2a} , the central signal ($+1/2 \leftrightarrow -1/2$ of T_{V2a} overlapped with V_{Si}^-), and the signal of $-1/2 \leftrightarrow -3/2$ of T_{V2a} . The first 180° pulse (width 80 ns) is strong enough to invert one of the three signals when the magnetic field is set to the signal, however is not sufficient to flip the other two signals, simultaneously. The intensity of the echo of 3-pulse inversion recovery was measured as a function of the magnetic field strength without ELDOR pulse (Fig. 17(c)) and with applying the ELDOR pulse (Fig. 17(a) and (b)). Although the microwave pulses have the excitation bandwidth exceeding the linewidth of the signals, the resolution of the conventional EPR is achieved by using a large window width for integrating the echo. The frequency (9.635 GHz and 9.775 GHz) and the width of the ELDOR pulse are selected to achieve the flipping angle of $\sim 180^\circ$ for the $\pm 3/2 \leftrightarrow \pm 1/2$ transitions at the magnetic field of the central signal. Without applying ELDOR pulse, we obtained the spectrum shown in Fig. 17(c) which is inverted one of the spectrum shown in Fig. 14(a). We note that the ELDOR pulses at 9.635 GHz and 9.775 GHz did cause a significant change of the central signal. By using the 180° ELDOR pulse of 9.635 GHz, the emission ($p(+1/2) \gg p(-1/2)$) of $+1/2 \leftrightarrow -1/2$ transition of T_{V2a} is added to the inverted signal of V_{Si}^- and the amplitude of the negative signal at the central line is strongly increased. By using the 180° ELDOR pulse of 9.775 GHz, the enhanced absorption ($p(+1/2) \gg p(-1/2)$) of the $+1/2 \leftrightarrow -1/2$ transition of T_{V2a} dominates over the inverted signal of V_{Si}^- . Thus, in Fig. 17(a), the central line is the pure signal of the $+1/2 \leftrightarrow -1/2$ transition of T_{V2a} .

In the field-swept spectra, the effect of the ELDOR pulse on the outer signals is somewhat more complicated. In the case of the ELDOR pulse of 9.635 GHz, the low

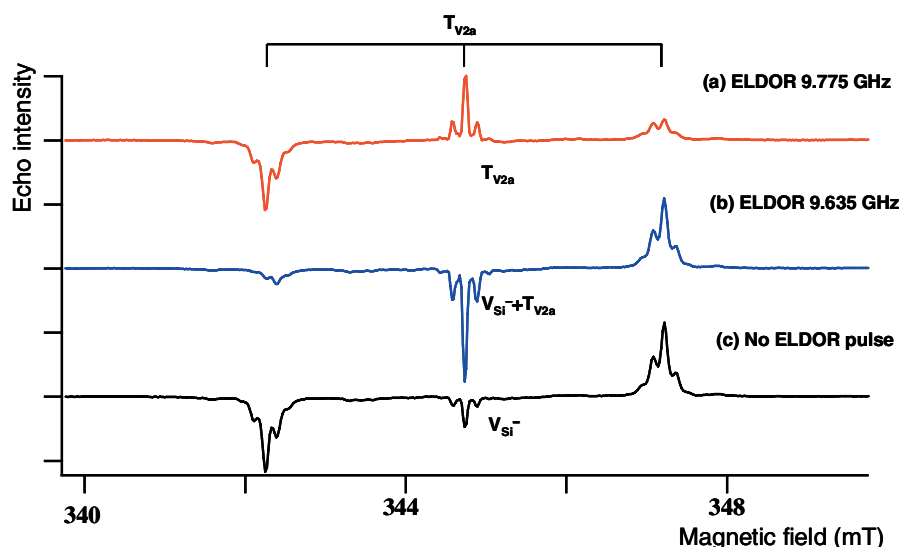


Figure 17 (online colour at: www.pss-b.com) Echo-detected EPR spectrum. The intensity of the 3-pulse inversion recovery was monitored as a function of the magnetic field.

field line corresponding to the $+3/2 \leftrightarrow +1/2$ transition was affected. At the magnetic field, at which the $+3/2 \leftrightarrow +1/2$ transition is resonant to 9.705 GHz, the $+1/2 \leftrightarrow -1/2$ transition is within the bandwidth of the ELDOR pulse of 9.635 GHz. The 180° pulse of 9.705 GHz at $t = 0$ inverts the polarization of the $+3/2 \leftrightarrow +1/2$ signal from the strong stimulated absorption $p(+3/2) \ll p(+1/2)$ to the strong stimulated emission $p(+3/2) \gg p(+1/2)$. This large population difference is decreased by the ELDOR pulse at $t = 1 \mu\text{s}$ which transfers the population of $-1/2$ level to $+1/2$ level. In the case of the ELDOR pulse of 9.775 GHz, the high field line corresponding to the $-1/2 \leftrightarrow -3/2$ transition was affected. At the magnetic field at which the $-1/2 \leftrightarrow -3/2$ transition is resonant to 9.705 GHz, the $+1/2 \leftrightarrow -1/2$ transition is flipped by the ELDOR pulse of 9.775 GHz. Thus, the population difference $p(-1/2) \ll p(-3/2)$ after the 180° pulse of 9.705 GHz was nearly cancelled by the ELDOR pulse at 9.775 GHz which transfers the population of $+1/2$ level to $-1/2$ level.

We note that both the line position (or the g -value) and the ^{29}Si HF structure of the $+1/2 \leftrightarrow -1/2$ transition of $T_{V_{2a}}$ is similar to those of V_{Si}^- as already known from the spin-Hamiltonian parameters determined from the fit of the outer lines. It should be noted that the line width of the $+1/2 \leftrightarrow -1/2$ transition of $T_{V_{2a}}$ is smaller than that of the outer lines and the ^{29}Si HF structure of second-nearest neighbours is more clearly observed for the signal of the $+1/2 \leftrightarrow -1/2$ transition than for the outer lines. Thus, the distribution of the zero-field splitting (D) contributes significantly to the line broadening of the outer lines.

In the third place, the Rabi oscillations (nutations) of $-3/2 \leftrightarrow -1/2$ and $+3/2 \leftrightarrow +1/2$ transitions, respectively, of $T_{V_{2a}}$ driven by the ELDOR pulses at 9.635 GHz and 9.775 GHz, respectively were measured by monitoring the polarization of the $+1/2 \leftrightarrow -1/2$ transition. The magnetic field was fixed at the central signal of Fig. 14.

In pulsed experiments, the behaviour of the magnetization is described using a coordinate system rotating with the microwave frequency around the external magnetic field ($z||B_0$, $x||B_1$). At the resonance condition, the microwave pulse rotates the magnetization around the x -axis through the angle

$$\theta(t_p) = (2\pi g \beta_e B_1 / h) t_p = \omega_n t_p$$

here, t_p is the pulse width, B_1 the microwave rotating field, ω_n the nutation frequency. The flipping by the microwave pulse changes the z -component of the magnetization which is related to the population difference of the two levels between which transition is induced. For the usual case starting from thermal equilibrium ($M_z = M_0$), the oscillation of the z -component of the magnetization is

$$M_z \propto M_0 \cos(\omega_n t_p).$$

In our case, we start from large $|M_z|$ ($|M_z| \gg M_0$), with the sign either positive (absorption) or negative (emission) due to polarization, $p(+1/2) \sim p(-1/2) \gg p(+3/2)$, $p(-3/2)$. The oscillation of M_z corresponding to the $-1/2 \leftrightarrow -3/2$ transi-

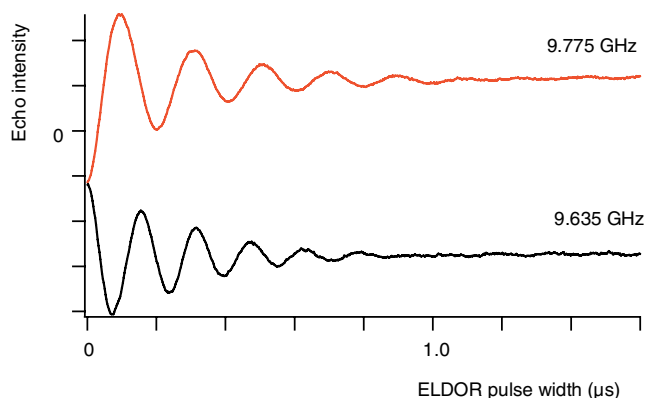


Figure 18 (online colour at: www.pss-b.com) Rabi oscillations of the $-1/2 \leftrightarrow -3/2$ and $+3/2 \leftrightarrow +1/2$ transitions, respectively, at the ELDOR frequency of 9.635 GHz and 9.775 GHz, respectively. The signal height of the echo signal of 3-pulse inversion recovery (9.705 GHz) of the $+1/2 \leftrightarrow -1/2$ transition was measured as a function of the pulse width of the ELDOR pulse.

tion by using the ELDOR pulse of 9.635 GHz or that corresponding to the $+3/2 \leftrightarrow +1/2$ transition using the ELDOR pulse of 9.775 GHz causes the oscillation of the population difference between the $+1/2$ and $-1/2$ levels. The population difference between the $+1/2$ and $-1/2$ levels is directly related to the signal height of the $+1/2 \leftrightarrow -1/2$ transition of $T_{V_{2a}}$. Thus, the Rabi oscillations of $-1/2 \leftrightarrow -3/2$ (9.635 GHz) and $+3/2 \leftrightarrow +1/2$ (9.775 GHz) transitions are monitored by measuring the echo signal of the $+1/2 \leftrightarrow -1/2$ transition (9.705 GHz).

The height of the 3-pulse echo at the magnetic field of the central signal was measured as a function of the pulse width of the ELDOR pulse (Fig. 18). The Rabi oscillations were observed for $\sim 1 \mu\text{s}$. In Fig. 18, the signal height at zero pulse width (i.e. ELDOR pulse off) corresponds to the height of the inverted signal of V_{Si}^- . The fact that the induced signal exhibits the Rabi oscillations of the $-3/2 \leftrightarrow -1/2$ and $+3/2 \leftrightarrow +1/2$ transitions confirms that the signal of the $+1/2 \leftrightarrow -1/2$ transition is indeed induced.

The difference of the nutation frequency for the two ELDOR frequencies 9.635 GHz and 9.775 GHz is likely to be caused by the difference of B_1 for the two frequencies in the pulsed ELDOR setup.

4 Divacancy In silicon, positively and negatively charged divacancies, $[VV]^+$ and $[VV]^-$, have been identified by EPR to have C_{2h} symmetry with $S = 1/2$. Removing two adjacent Si atoms produces six dangling bonds (a , b , d , a' , b' , and d'). Unrelaxed divacancy of D_{3d} symmetry has two singlets a_{1g} and a_{1u} in the valence band, and two doublets e_g and e_u in the energy gap, with e_g higher than e_u . Since the e_u level is partially occupied ($V_2^+ : e_u^1$, $V_2^- : e_u^3$), a Jahn–Teller distortion, which reconstructs pair bonds between a and d , a' and d' , lowers the symmetry to C_{2h} . In both $[VV]^+$ and $[VV]^-$, the unpaired electron is localized mainly on atoms b and b' in the mirror plane of C_{2h} symmetry. The spin density η_i^2 and the sp-hybrid ratio β_i^2/α_i^2 on

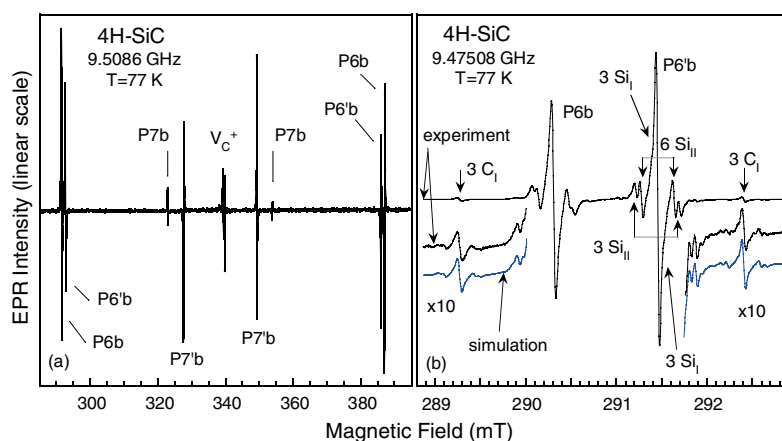


Figure 19 (online colour at: www.pss-b.com) (a) EPR spectra of the P6/P7 centers in as-grown HPSI 4H-SiC substrates measured for $\mathbf{B}||c$ at 77 K under illumination with light of photon energies $\sim 2\text{--}2.8$ eV. (b) Part of the P6 spectra in electron-irradiated and annealed (850 °C) HPSI 4H-SiC recorded at 77 K for $\mathbf{B}||c$, showing the HF structures of 3 nearest neighbors C_I and 9 second neighbors Si_{II} of V_{Si} . The HF structure due to the interaction with 3 nearest Si neighbors of V_C is not resolved. The simulations using the HF parameters and line width obtained from experiments are plotted for comparison. Detailed structures of the HF lines can be seen in $\times 10$ scale inserts of experimental and simulated spectra. (Son et al., Phys. Rev. Lett. **96**, 055501 (2006). Copyright (2006) by the American Physical Society) [42].

these atoms (b and b') are 27.5%, 7.5 for $[VV]^+$ and 24.6%, 4.8 for $[VV]^-$ [34–36].

The neutral vacancy in silicon is diamagnetic ($S = 0$). It should be noted that, if $[VV]^0$ of D_{3d} symmetry had taken non-orbitally-degenerate $^3A_{2g}$ ($S = 1$) state arising from electronic configuration e_u^2 , then no Jahn–Teller distortion is expected. The neutral divacancy in diamond has $S = 1$, however, the symmetry is lowered to C_{2h} [4]. The unpaired electron is mainly localized on four atoms (a , d , a' , and d') which are not in the mirror plane, with $\eta_i^2 = 20\%$ and $\beta_i^2/\alpha_i^2 = 9$.

The P6/P7 centers ($S = 1$) in 4H-SiC have been established to be originating from the ground state of the neutral divacancy $[V_{Si}V_C]^0$, the closest pair of the silicon vacancy (V_{Si}) and the carbon vacancy (V_C), through the cooperation between the *first principles* calculations which supplied the predicted HF parameters and the careful EPR measurements of the ^{13}C HF lines, both the angular dependence and the intensity relative to the primary lines. Four configurations (hh , kk with C_{3v} symmetry, hk , kh with C_{1h} symmetry) are distinguishable by EPR.

The divacancy was suggested as a model for the P6/P7 EPR centers in heat treatment 6H-SiC in the early 1980s by Vainer and Il'in [37]. However, the identification was based only on the observed symmetry of the centers (C_{1h} for P6 and C_{3v} for P7). Since light illumination was needed for detecting the spectra, the centers were believed to be related to the excited triplet states of the divacancy [37]. These centers are also commonly detected in n-type 6H-SiC by ODMR [38] or in high-purity semi-insulating (HPSI) 4H- and 6H-SiC substrates by EPR [39, 40].

In a later study using MCDA (magnetic circular dichroism of the absorption)-detected EPR and *first principles* calculations by Lingner and co-workers [41], P6/P7

EPR spectra in 6H-SiC were claimed to be the carbon-antisite carbon-vacancy pair in the double positive charge state ($[C_{Si}V_C]^{2+}$).

Figure 19(a) shows the P6/P7 spectra in as-grown HPSI 4H-SiC substrates detected at 77 K for the magnetic field $\mathbf{B}||[0001]$ under illumination of light of photon energies in the range 2.0–2.8 eV. In the 4H polytype, there are two configurations with C_{3v} symmetry (P6b and P6'b) and two configurations with C_{1h} symmetry (P7b and P7'b). The P6/P7 centers have the same g -value $g = 2.003$ and slightly different fine-structure parameters D and E (in unit of 10^{-4} cm^{-1}): $D(\text{P6b}) = D(\text{P7b}) = 447$, $D(\text{P6'b}) = 436$, $D(\text{P7'b}) = 408$, $E(\text{P7b}) = 90$ and $E(\text{P7'b}) = 10$. The angle between the principal axis of the fine structure tensor and the c axis for P7b and P7'b is 109.5° and 109° , respectively. Recently, detailed HF structures of the P6 and P7 centers in 4H- and 6H-SiC have been observed [15, 43]. Typical HF structures for parts of the P6b and P6'b spectra in 4H-SiC are shown in Fig. 19(b). As shown in the figure, the large splitting HF lines are from the interaction with three nearest C neighbours of V_{Si} . The inner HF lines are due to the interaction with nine next-nearest Si neighbors, of which three Si atoms on the bonds along the c -axis has a slightly larger splitting. The HF interaction with three nearest Si neighbours of V_C is small and not resolvable. The principal values of the HF tensors determined for the P6b, P6'b and P7'b centers in 4H-SiC are shown in Table 4. The observed HF constants are in good agreement with the values obtained from the supercell calculations of the neutral divacancy model [15, 44]. The P6/P7 centers were therefore identified as different configurations of the neutral divacancy ($[V_{Si}V_C]^0$). Comparing the observed HF constants with the calculated values for different configurations, it was possible to assign the P6b and P6'b centers to

Table 4 Principal values of the HF tensors (in unit of mT) of the neutral divacancy in 4H-SiC. The HF constants due to the interaction with 9 next nearest Si neighbours of V_C are ~ 0.3 – 0.4 mT and not included. η_i^2 is the fraction of the total spin density that is localized at one of the neighboring C or Si atoms. β_i^2/α_i^2 is the sp-hybridization ratio. θ is the angle between the principal A_{zz} axis and the c -axis (see Fig. 20). The values are taken from Ref. [15].

center symmetry	atom	HF tensors			η_i^2 (%)	β_i^2/α_i^2	θ
		A_{xx}	A_{yy}	A_{zz}			
$[V_{Si}(h) - V_C(h)]^0$ P6b (C_{3v})	C_{1-3}	1.89	1.78	3.93	20.1	9.7	107°
	Si_{1-3}	~ 0.1	~ 0.1	~ 0.1	0.6	~ 0	
	total				60.5		
$[V_{Si}(k) - V_C(k)]^0$ P6'b (C_{3v})	C_{1-3}	1.68	1.61	3.71	19.7	10.4	107°
	Si_{1-3}	~ 0.1	~ 0.1	~ 0.1	0.6	~ 0	
	total				59.3		
$[V_{Si}(k) - V_C(h)]^0$ P7'b (C_{1h})	C_1	1.86	1.86	3.93	19.9	9.5	2°
	$C_{2,3}$	1.71	1.61	3.89	21.2	10.9	110°
	total				62.3		

the axial C_{3v} configurations at the hexagonal and cubic sites [P6b: $V_{Si}(h) - V_C(h)$, P6'b: $V_{Si}(k) - V_C(k)$] and the P7b and P7'b centers to the monoclinic C_{1h} configurations, $V_{Si}(h) - V_C(k)$ and $V_{Si}(k) - V_C(h)$, respectively [15]. Figure 20 shows schematic atomic models for the $[V_{Si}V_C]^0$ centers. Using the linear combination of atomic orbital analysis, the spin density on a nearest C neighbor is determined as: ~ 1.8 – 1.9% on the s-orbital and ~ 18 – 19% on the p-orbital for P6b, P6'b and P7'b. The sp-hybrid ratio is $(\beta^2/\alpha^2) \sim 10$ for all the configurations. The total spin density on the three nearest C neighbors of the neutral divacancy is $\sim 60\%$ for the C_{3v} configuration (P6b/P6'b) and $\sim 62\%$ for the C_{1h} configuration (P7'b). In the C_{3v} configurations, the spin density is equally distributed among the three nearest C neighbors and the direction of p-orbitals ($\theta = 107^\circ$) with respect to the vacancy-vacancy direction (see Fig. 20) is slightly smaller than the tetrahedral angle (109.5°). In the case of P7'b center, the localization of spins at the C atom along the c -axis is slightly smaller than that at the other two C atoms on the inclined bonds. In both C_{3v} and C_{1h} configurations, the spin localization on three nearest Si neighbors of V_C is negligible ($\sim 1\%$). With electrons on the e level arising from C dangling bonds of V_{Si} ,

the spin localization for the neutral divacancy is similar to that of V_{Si}^- : ~ 60 – 62% on three nearest C neighbors of V_{Si} in the divacancy and ~ 62 – 65% on four nearest C neighbors for V_{Si}^- .

In as-grown samples, the observation of the P6/P7 centers requires illumination with light of photon energies larger than ~ 1.1 eV. However, in some irradiated 4H- and 6H-SiC samples, the spectra could be detected in the dark even at low temperatures (1.5 – 8 K) [15, 45]. This confirms that the spectra are related to the ground state, in agreement with the supercell calculations of the neutral divacancy [15, 39]. In the divacancy, three C dangling bonds and three Si dangling bonds create six defect levels. In the axial configuration with C_{3v} symmetry, two a_1 levels fall in the valence band and two double generate e levels lie in the band gap. The lower e level arises from the C dangling bonds of the Si vacancy and the upper e level arises from the Si dangling bonds of the C vacancy. In the neutral charge state, there are six electrons, four of them fill the two resonance a_1 levels in the valence band and the other two occupy the lower degenerate e level, giving rise to the spin $S = 1$ for the ground state. In 4H-SiC, the calculations found the (+/0) and (0/−) levels to be at ~ 0.5 eV and ~ 1.4 eV above the valence band, respectively [15, 44]. Recent EPR studies in irradiated HPSI 4H-SiC substrates [46] show that in the dark at 77 K only the V_C^+ signal was observed. However, increasing the temperature to 293 K while keeping the sample in darkness, the $[V_{Si}V_C]^0$ signal could be weakly detected. This suggests that the (0/−) level of $V_C V_{Si}$ may lie slightly below the (+/0) level of V_C at $\sim E_V + 1.47$ eV [47] so that at room temperature it could be partly thermally ionized. Consequently, a part of the total concentration of the divacancy is changed to the neutral charge state and could be detected. This EPR estimation is close the theoretical prediction of the (0/−) level at $\sim E_V + 1.4$ eV. Recently, the divacancy has been identified as a prominent defect responsible for the semi-insulating properties in HPSI 4H-SiC substrates with thermal activa-

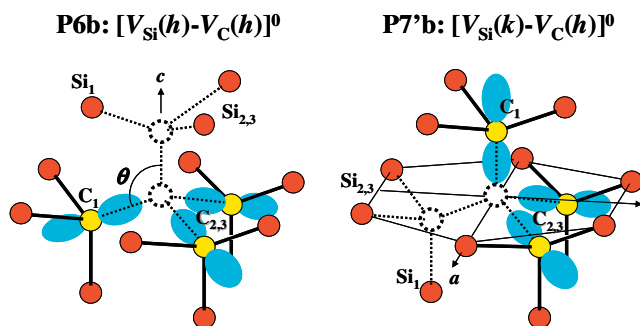


Figure 20 (online colour at: www.pss-b.com) Atomic structures of divacancy centers in 4H-SiC.

tion energies of ~ 1.5 – 1.6 eV, which may be associated to the single acceptor level (0/−) of $[V_{Si}V_C]$ [46].

The no-phonon lines related to the P6 centers in irradiated n-type 6H-SiC substrates were found to reach their maximum intensity after annealing at ~ 900 °C and to be disappeared after an 1200 °C anneal [48]. In electron-irradiated HPSI 4H- and 6H-SiC substrates, the EPR signals of the divacancy were annealed out at higher temperatures (~ 1400 °C), whereas in as-grown HPSI materials with low concentrations of defects and residual impurities (N and B) their intensities only started decreasing after annealing at 1600 °C [46].

In 6H-SiC, the relation between the P6/P7 triplet states and the no-phonon lines of the near-infrared photoluminescence (PL) band has been confirmed (P6a–c: 1.075, 1.048 and 1.011 eV; P7a–c: 1.049, 1.030 and 0.999 eV) [41]. In 4H-SiC samples with strong EPR signals of the neutral divacancy, five strong absorption lines were also detected at 0.9975, 1.0136, 1.0507 and 1.0539 eV [49]. These lines were also weakly detected in PL. Weak PL emissions may be the reason why the P6/P7 centers in 4H-SiC have not been detected by optical detection of magnetic resonance. In 4H-SiC, the correlation between these no-phonon lines and the P6/P7 EPR centers has not been confirmed.

5 Antisites and antisite–vacancy pairs Antisites and antisite–vacancy (AV) pairs are fundamental native defects in compound semiconductors. In SiC, both carbon antisite (C_{Si}) and silicon antisite (Si_C) can be easily formed [50, 51]. For AV pairs, carbon AV pairs ($C_{Si}V_C$) can be stable [52, 53].

Carbon antisite is expected to be one of the most common and abundant defects in SiC, because of its lowest formation energy among various native defects [50, 51]. However, the presence of C_{Si} has not been clear yet, because the *first principles* theory [50, 51] predicted that C_{Si} has no gap states and it will be invisible for any electrical and optical measurements. Recently, however, in neutron irradiated 6H-SiC after 700 °C anneal, a C_{Si} center ($S = 1/2$) was reported by Baranov et al. [54]. A single strong ^{13}C HF interaction ($A_{||} = 8.1$ mT, $A_{\perp} = 3.0$ mT, see Fig. 21(a)) was detected in the EPR spectrum of this center, suggesting the contribution of a C_{Si} atom to this HF interaction. However, this is not a final proof of the C_{Si} center, because carbon AV pairs [55] (see the text in later) and divacancies [56] can show similar strong ^{13}C HF interactions when they are positively charged. Nevertheless, C_{Si} is a particularly interesting defect, because it is the “anion” antisite in SiC. An anion antisite in GaAs (As_{Ga} , the EL2 center) exhibits a famous bistability [57], in which the As_{Ga} atom can stay either a four-fold-coordinated position or a three-fold-coordinated position. This bistability is accompanied with a change in the electrical and optical activity of the antisite center. By analogy with this phenomenon, an inactive C_{Si} center (sp^3 -coordinated position) may transform into an active one (sp^2 -coordinated position) in SiC. The Baranov’s center may be explained by the latter one.

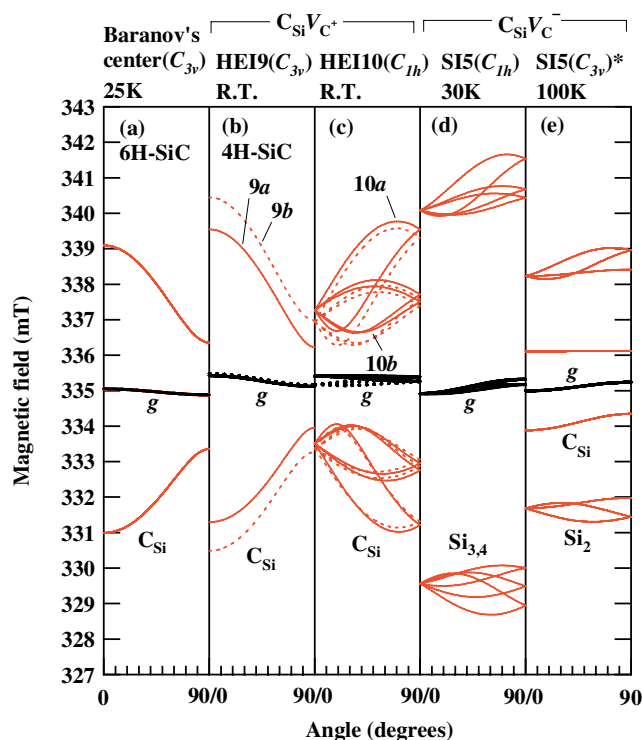


Figure 21 (online colour at: www.pss-b.com) Angular maps for carbon antisite-related EPR centers. (a) Baranov’s center in 6H-SiC [54], (b) HEI9 centers or c -axial pairs of $C_{Si}V_C^+$ in 4H-SiC [55], (c) HEI10 centers or basal pairs of $C_{Si}V_C^-$ in 4H-SiC [55], (d) SI5 center or c -axial pairs of $C_{Si}V_C^-$ in LT configuration and (e) in HT configuration [53]. These maps were simulated on “EPR in Semiconductors” (<http://www.kc.tsukuba.ac.jp/div-media/epr/>) using a microwave frequency of 9.400 GHz and B rotation from [0001] to $[11\bar{2}0]$ (from 0° to 90°). Primary and $^{13}C/^{29}Si$ HF lines are denoted by, for example, “g” and “ C_{Si} ”, respectively. “ Si_2 ” and “ $Si_{3,4}$ ” atoms are three Si neighbors of V_C . * EPR parameters are gradually changed as a function of the temperature.

Still we may not understand a complete nature of C_{Si} in SiC, so that further studies will be necessary from experimental and theoretical view points.

On the other hand, silicon antisite attracts less attention than C_{Si} , because their influences will be limited to a heavily p-doped region. All its gap levels are close to the valence band edge [50]. There is only one probable assignment for the Si_C center; a series of the H centers ($E_V + 0.18 \sim 0.51$ eV) in the deep level transient spectroscopy (DLTS) spectrum of neutron irradiated 3C-SiC may originate from Si_C in different charge states [50]. For the Si_C^+ center ($S = 1/2$), a detectable ^{29}Si HF interaction ($A_{||} = 3.2$ – 3.4 mT, $A_{\perp} = 0.7$ – 0.9 mT) due to a Si_C atom was predicted by *first principles* theory [16]. However, such a signature was not reported for any p-type samples.

An AV pair is a fundamental native defect, because it is a counterpart of a monovacancy in compound semiconductors [53]. For example, in an AB compound semiconductor, an A vacancy and a B antisite– B vacancy pair can

be transformed from one to another by simply moving a B atom. Carbon AV pair (anion AV pair in SiC) is expected to be important in p-type and SI SiC. In p-type SiC, a $C_{Si}V_C$ pair is energetically rather favorable than a V_{Si} [52, 58]. This relationship is also true for some SI SiC substrates, depending on their Fermi levels [46, 52, 53]. Such a trend is commonly seen in anion AV pairs in GaAs [59] and in ZnO [60], according to theoretical calculations. However, the presence of AV pairs has been confirmed only in SiC. By means of a combination of EPR and *first principles* calculation, the HEI9/10 centers ($S = 1/2$) in irradiated p-type 4H-SiC were identified as the $C_{Si}V_C^+$ pairs [55]. Figure 22 shows schematic atomic structures of the $C_{Si}V_C$ centers. Their typical spectrum is shown in Fig. 2(b). Since there are four inequivalent configurations (kk , hh , kh , and hk) for any pairing center in 4H-SiC, four types of HEI9/10 (9a, 9b, 10a, and 10b) can be resolved. The HEI9a and 9b centers correspond to hh and kk configurations (c -axial pairs, C_{3v} symmetry), while HEI10a and 10b are kh and hk ones (basal pairs, C_{1h} symmetry). All of them exhibit a single strong ^{13}C HF interaction due to a C_{Si} atom (Fig. 21(b) and (c)). Their ^{13}C HF interactions ($A_{||} = 8.2$ – 9.9 mT, $A_{\perp} = 2.2$ – 3.7 mT) indicate a very strong localization (55 – 58%) and a very strong p-character ($\beta^2/\alpha^2 = 12$ – 16) on the C_{Si} atom as shown in Table 5. The 2nd and 3rd largest HF interactions arise from ^{29}Si atoms in the V_C side and outer shells. Accordingly, the HEI9/10 EPR spectrum involves many ^{29}Si HF satellites ($A = 1.7$ – 2.9 mT). The $C_{Si}V_C^+$ centers were often more abundant than V_C^+ (see Fig. 2(b)). However, their EPR signals were greatly underestimated at low temperatures owing to a strong saturation effect. In 6H-SiC, there are no reports for the relevant centers, however, the Baranov's center mentioned above [54] may be consistent with a c -axial $C_{Si}V_C^+$ pair in 6H-SiC, because we can find a close similarity between Figs. 21(a) and (b). In 4H-SiC, the electronic levels (the a and a' levels for c -axial and basal pairs, respectively) of $C_{Si}V_C^+$ were deduced to be $E_V + 1.4$ – 1.5 eV ($E_V + 1.2$ – 1.3 eV in theory) [55]. The $C_{Si}V_C^+$ centers are annealed out at 1100 – 1200 °C in irradiated SiC, which is almost the same behavior as V_C^+ [55].

Other charge states of $C_{Si}V_C$ will be also detectable in EPR or optical measurements. The SI5 EPR center (the

Table 5 Orbital parameters of carbon antisite-related centers in 4H-SiC calculated from experimental ^{13}C and ^{29}Si HF tensors [53, 55]: The spin density η_i^2 , the sp hybrid ratio β_i^2/α_i^2 , and the direction of the p-orbital θ with respect to the Cartesian coordinate (see Fig. 22 for the definition).

center, symmetry	atom	η_i^2 (%)	β_i^2/α_i^2	θ
$C_{Si}V_C^+$				
$[C_{Si}(h) - V_C(h)]^+$	C_{Si}	55.1	16.4	0°
HEI9a (C_{3v})				
$[C_{Si}(k) - V_C(k)]^+$	C_{Si}	58.6	12.6	0°
HEI9b (C_{3v})				
$[C_{Si}(k) - V_C(h)]^+$	C_{Si}	56.8	15.4	109°
HEI10a (C_{1h})				
$[C_{Si}(h) - V_C(k)]^+$	C_{Si}	56.0	16.1	109°
HEI10b (C_{1h})				
$C_{Si}V_C^-$				
SI5 (C_{1h}), 30 K	$Si_{3,4}$	30.3	3.5	111°
	total		60.6	
SI5 (C_{3v}), 100 K	Si_2	17.6	3.2	108°
	C_{Si}	5.3	2.7	0°
	total		22.9	

SI-5 center in SI 4H-SiC [61] or the HEI4 center in irradiated n-type 4H-SiC [62]) was assigned to a c -axial $C_{Si}V_C^-$ center ($S = 1/2$) [53]. In the negative charge state, an unpaired electron occupies a doubly-degenerate level (the e level) originating from Si neighbors of V_C . As a result, a strong ^{29}Si HF interaction is observed in the SI5 EPR spectrum (Fig. 21(d)), in contrast with the positive charge state already mentioned. Furthermore, there are two possible Jahn–Teller distorted configurations with C_{1h} symmetry, which are named as “LT (low-temperature)” and “HT (high temperature)” configurations [53]. In the LT one, an unpaired electron is localized on two Si neighbors of V_C ($Si_{3,4}$, mirror symmetric with respect to $(11\bar{2}0)$), while in the HT one, it considerably extends over a C_{Si} atom and outer parts (see Table 5). The HT configuration is strongly temperature dependent, and a thermal average causes an apparent C_{3v} symmetry as shown in Fig. 21(e). Above 150 K, the HT spectrum is hardly observed due to the signal broadening. The transition between the LT and HT configurations occurs at around 50 K. The ^{29}Si HF interaction of the LT configuration ($A_{||} = 13$ mT, $A_{\perp} = 10$ mT) indicates that the degree of localization (60.6%) and the sp -hybridization ratio (3.5, see Table 5) are quite similar to those of V_C^- (Table 3). It should be mentioned that the SI5 center is extremely sensitive to photo illumination. In SI and n-type 4H-SiC ($E_F \sim E_C - 1.1$ eV), the $C_{Si}V_C^-$ centers ($S = 0$) are dominantly formed, and they can be easily converted into $C_{Si}V_C^+$ by photo excitation of electrons to the conduction band [53]. This causes a drastic increase in the SI5 signal as is seen in Fig. 2(a). Such a photo sensitivity cannot be seen in the HEI9/10 signals (Fig. 2(b)). Judging from the photo response of the SI5 center, the $(-/-2)$ and $(0/-)$ ionization levels were deduced to be $E_C - 1.05$ –

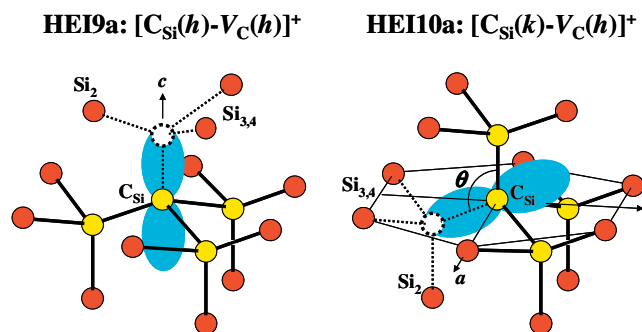


Figure 22 (online colour at: www.pss-b.com) Atomic structures of carbon antisite–vacancy pairs in 4H-SiC.

1.35 eV and $E_C - 1.24 - 1.4$ eV, respectively [46] ($E_C - 0.9$ eV and $E_C - 1.0$ eV in theory, respectively [53]). Due to these two levels, the $C_{Si}V_C$ pairs can contribute to the SI mechanism that exhibits a carrier activation energy of 1.1–1.3 eV [46].

In the last place of this section, we mention that the $C_{Si}V_C$ centers will be detectable in other spectroscopic techniques. In electron irradiated n-type 6H-SiC after 1000 °C anneal, the presence of a c -axial $C_{Si}V_C^-$ pair was strongly suggested by two-dimensional angular correlation of positron annihilation technique [63]. The basal $C_{Si}V_C^-$ pairs were not observed in this study, and in n-type 4H-SiC, too [53]. The reason why the basal pairs are hidden in n-type samples remains an unresolved problem.

6 Conclusion Vacancy-related defects such as monovacancy, divacancy, and antisite-vacancy pairs in 4H-SiC have been studied by EPR. The comparison of the obtained HF parameters with those predicted from the *first principles* calculations played a critical role in identification of $V_C^+(h)/V_C^+(k)$, $V_C^-(h)$, $[V_{Si}V_C]^0$, $[C_{Si}V_C]^+$ and $[C_{Si}V_C]^-$.

The measurements of the angular dependence of the $^{13}C/^{29}Si$ satellite lines from the nearest-neighbors, which are crucial for identification, have revealed the detailed geometric and electronic structures.

From the orbital parameters estimated from the $^{13}C/^{29}Si$ hyperfine tensors by using a simple LCAO model, the following points, which were predicted to a considerable extent by theoretical studies, have been evidently confirmed.

(1) The localization of spin densities on the nearest-neighbors ($\eta_{shell-I}^2$) of monovacancies in 4H-SiC is larger than that in silicon and significantly smaller than that in diamond.

(2) The positively charged vacancy (V_C^+) has slightly larger localization and higher p-character than the negatively charged vacancy (V_C^-), similarly to V^+ and V^- in silicon; $\eta_{shell-I}^2$ and the sp-hybrid ratio β^2/α^2 are 68%, 5.3–5.9 for $V_C^+(h)/V_C^+(k)$, 61%, 3.6 for $V_C^-(h)$, and 58%, 5.6 and 54.6%, 3.4 for V^+ and V^- in silicon [5, 6, 19].

(3) Similar to V^+ and V^- in silicon, Jahn–Teller distortion is significant for both $V_C^+(h)/V_C^+(k)$ and $V_C^-(h)$ in 4H-SiC, and hence $V_C^-(h)$ takes low spin configuration ($S = 1/2$). On the other hand the electron–electron repulsion favors the high spin configuration for V_{Si}^- ($S = 3/2$), similar to V^- in diamond. The distance 3.08 Å between the nearest-neighbors of unrelaxed vacancy is not strikingly larger than Si–Si bond length (2.35 Å in silicon), however, fatally larger than C–C bond length (1.54 Å in diamond). Thus, silicon dangling bonds in V_C form pairing bonds easily while carbon dangling bonds in V_{Si} are likely to be parted from each other [27]. It should be noted that the distance between the nearest-neighbors of unrelaxed vacancy in 4H-SiC is shorter than that of silicon (3.83 Å) and longer than that of diamond (2.52 Å).

(4) The Jahn–Teller distortion is remarkably different between $V_C^+(h)$ (C_{3v}) and $V_C^+(k)$ (C_{1h}) in 4H-SiC. The slight difference in the small distortion from tetrahedral structure between $V_{Si}^-(h)$ and $V_{Si}^-(k)$ has been revealed.

(5) The sp-hybrid ratio (~ 12) for the nearest-neighbor carbon atoms in V_{Si}^- is significantly higher than that (~ 5) of the nearest-neighbor silicon atoms in V_C^+ . The large p-character in V_{Si}^- is ascribed to the outward displacement of carbon atoms forming more sp²-like bonds with the next-nearest-neighbors which results in more p-like contribution to the wave function of the unpaired electron.

(6) The neutral divacancy $[V_{Si}V_C]^0$ in 4H-SiC, in which the unpaired electrons are mainly confined on carbon atoms of nearest-neighbors of V_{Si} , takes high-spin state ($S = 1$), whereas Jahn–Teller distortion gives rise to the ground state of $S = 0$ for $[VV]^0$ in silicon. The localization ($\sim 60\%$) on the six nearest-neighbors (with negligibly small spin density on three silicon atoms) is smaller than that of $[VV]^0$ in diamond (82%) [4] and slightly larger than that in silicon (59.3% and 54.6 % for $[VV]^+$ and $[VV]^-$, respectively) [34].

Antisite–vacancy (AV) pairs, which are unique to compound semiconductors, have been identified.

The determination of the spin multiplicity of $T_{V_{2a}}$ to be $S = 3/2$ by the nutation method of pulsed EPR and pulsed ENDOR has revealed that $T_{V_{2a}}$ belongs to a family of V_{Si}^- . The assigning of $T_{V_{2a}}$ to V_{Si}^0 with $S = 1$ was misled by the missing of the central line of $T_{V_{2a}}$. It is demonstrated that the central line has been observed by the population transfer using pulsed ELDOR technique.

Acknowledgements Here we review our works from the experimentalist side. Our identification of point defects has been achieved with collaboration with theoretical groups, A. Gali (Budapest University of Technology and Economics) and M. Bockstedte (Universität Erlangen–Nürnberg). We would like to thank Dr. H. Hara (Bruker Biospin, Japan) for his help with the pulsed-ELDOR experiments.

References

- [1] J. Isoya, H. Kanda, Y. Uchida, S. C. Lawson, S. Yamasaki, H. Itoh, and Y. Morita, *Phys. Rev. B* **45**, 1436 (1992).
- [2] J. Isoya, H. Kanda, J. R. Norris, J. Tang, and M. K. Bowman, *Phys. Rev. B* **41**, 3905 (1990).
- [3] D. J. Twitchen, M. E. Newton, J. M. Baker, O. D. Tucker, T. R. Anthony, and W. F. Banholzer, *Phys. Rev. B* **54**, 6988 (1996).
- [4] D. J. Twitchen, M. E. Newton, J. M. Baker, T. R. Anthony, and W. F. Banholzer, *Phys. Rev. B* **59**, 12900 (1999).
- [5] G. D. Watkins, in: *Radiation Damage in Semiconductors*, edited by P. Baruch (Dunod, Paris, 1965), pp. 97–113.
- [6] M. Sprenger, S. H. Muller, E. G. Sieverts, and C. A. J. Ammerlaan, *Phys. Rev. B* **35**, 1566 (1987).
- [7] St. G. Müller, M. F. Brady, W. H. Brixius, R. C. Glass, H. D. McHobgood, J. R. Jenny, R. T. Leonard, D. P. Malta, A. R. Powell, V. F. Tsvetkov, S. T. Allen, J. W. Palmour, and C. H. Carter, Jr., *Mater. Sci. Forum* **433–436**, 39 (2003) and references therein.
- [8] A. Ellison, B. Magnusson, N. T. Son, L. Storasta, and E. Janzén, *Mater. Sci. Forum* **433–436**, 33 (2003).
- [9] A. I. Veinger, A. G. Zabrodskii, G. A. Lomakina, and E. N. Mokhov, *Fiz. Tverd. Tela* **28**, 1659 (1984).

- [10] E. Rauls, M. V. B. Pinheiro, S. Greulich-Weber, and U. Gerstmann, *Phys. Rev. B* **70**, 85202 (2004).
- [11] S. Greulich-Weber, *phys. stat. sol. (a)* **162**, 95 (1997).
- [12] N. T. Son, A. Henry, J. Isoya, M. Katagiri, A. Gali, and E. Janzén, *Phys. Rev. B* **73**, 075201 (2006).
- [13] J. A. Weil, J. R. Bolton, J. E. Wertz, *Electron Paramagnetic Resonance* (John Wiley & Sons, New York, 1994).
- [14] T. Umeda, J. Isoya, N. Morishita, T. Ohshima, and T. Kamiya, *Phys. Rev. B* **69**, 121201(R) (2004).
- [15] N. T. Son, P. Carlsson, J. ul Hassan, E. Janzén, T. Umeda, J. Isoya, A. Gali, M. Bockstedte, N. Morishita, T. Ohshima, and H. Itoh, *Phys. Rev. Lett.* **96**, 055501 (2006).
- [16] M. Bockstedte, M. Heid, and O. Pankratov, *Phys. Rev. B* **67**, 193102 (2003).
- [17] T. Wimbauer, B. K. Meyer, A. Hofstaetter, A. Scharmann, and H. Overhof, *Phys. Rev. B* **56**, 7384 (1997).
- [18] N. Mizuochi, S. Yamasaki, H. Takizawa, N. Morishita, T. Ohshima, H. Itoh, T. Umeda, and J. Isoya, *Phys. Rev. B* **72**, 235208 (2005).
- [19] G. D. Watkins, *J. Phys. Soc. Jpn.* **18**(Suppl. II), 22 (1963).
- [20] H. Itoh, M. Yoshikawa, I. Nashiyama, S. Misawa, H. Okumura, and S. Yoshida, *IEEE Trans. Nucl. Sci.* **37**, 1732 (1990).
- [21] H. Itoh, A. Kawasuso, T. Ohshima, M. Yoshikawa, I. Nashiyama, S. Tanigawa, S. Misawa, H. Okumura, and S. Yoshida, *phys. stat. sol. (a)* **162**, 173 (1997).
- [22] N. Mizuochi, S. Yamasaki, H. Takizawa, N. Morishita, T. Ohshima, H. Itoh, and J. Isoya, *Phys. Rev. B* **68**, 165206 (2003).
- [23] E. Sörman, N. T. Son, W. M. Chen, O. Kordina, C. Hallin, and E. Janzén, *Phys. Rev. B* **61**, 2613 (2000).
- [24] N. Mizuochi, S. Yamasaki, H. Takizawa, N. Morishita, T. Ohshima, H. Itoh, and J. Isoya, *Phys. Rev. B* **66**, 235202 (2002).
- [25] Mt. Wagner, N. Q. Thinh, N. T. Son, W. M. Chen, E. Janzén, P. G. Baranov, E. N. Mokhov, C. Hallin, and J. L. Lindstrom, *Phys. Rev. B* **66**, 155214 (2002).
- [26] A. Zweitz, J. Furthmüller, and F. Bechstedt, *phys. stat. sol. (b)* **210**, 13 (1998).
- [27] A. Zweitz, J. Furthmüller, and F. Bechstedt, *Phys. Rev. B* **59**, 15166 (1999).
- [28] N. T. Son, P. N. Hai, and E. Janzén, *Phys. Rev. B* **63**, R201201 (2001).
- [29] N. T. Son, P. N. Hai, and E. Janzén, *Phys. Rev. Lett.* **87**, 045502 (2001).
- [30] T. Umeda, J. Isoya, N. Morishita, T. Ohshima, T. Kamiya, A. Gali, P. Deák, N. T. Son, and E. Janzén, *Phys. Rev. B* **70**, 235212 (2004).
- [31] V. Ya. Bratus, T. T. Petrenko, S. M. Okulov, and T. L. Petrenko, *Phys. Rev. B* **71**, 125202 (2005).
- [32] T. Umeda, Y. Ishitsuka, J. Isoya, N. T. Son, E. Janzén, N. Morishita, T. Ohshima, H. Itoh, and A. Gali, *Phys. Rev. B* **71**, 193202 (2005).
- [33] M. E. Zvanut, *J. Phys.: Condens. Matter* **16**, R1341 (2004).
- [34] G. D. Watkins and J. W. Corbett, *Phys. Rev.* **138**, A543 (1965).
- [35] J. G. de Wit, E. G. Sievertz, and C. A. J. Ammerlaan, *Phys. Rev. B* **14**, 3494 (1976).
- [36] E. G. Sievertz, S. H. Muller, and C. A. J. Ammerlaan, *Phys. Rev. B* **18**, 6834 (1978).
- [37] V. S. Vainer and V. A. Il'in, *Sov. Phys. Solid State* **23**, 2126 (1981).
- [38] N. T. Son, Mt. Wagner, E. Sörman, W. M. Chen, B. Mone-mar, and E. Janzén, *Semicond. Sci. Technol.* **14**, 1141 (1999).
- [39] W. E. Carlos, E. R. Glaser, and B. V. Shanabrook, *Physica B* **340–342**, 151 (2003).
- [40] N. T. Son, B. Magnusson, Z. Zolnai, A. Ellison, and E. Janzén, *Mater. Sci. Forum* **457–460**, 437 (2004) and references therein.
- [41] Th. Lingner, S. Greulich-Weber, J.-M. Spaeth, U. Gerstmann, E. Rauls, Z. Hajnal, Th. Frauenheim, and H. Overhof, *Phys. Rev. B* **64**, 245212 (2001).
- [42] N. T. Son, P. Carlsson, J. ul Hassan, E. Janzén, T. Umeda, J. Isoya, A. Gali, M. Bockstedte, N. Morishita, T. Ohshima, and H. Itoh, *Phys. Rev. Lett.* **96**, 055501 (2006).
- [43] N. T. Son, T. Umeda, J. Isoya, A. Gali, M. Bockstedte, B. Magnusson, A. Ellison, N. Morishita, T. Ohshima, H. Itoh, and E. Janzén, *Mater. Sci. Forum* **527–529**, 527 (2006).
- [44] A. Gali, M. Bockstedte, N. T. Son, T. Umeda, J. Isoya, and E. Janzén, *Mater. Sci. Forum* **527–529**, 523 (2006).
- [45] I. V. Ilyin, M. V. Muzafarova, E. N. Mokhov, V. I. Sankin, P. G. Baranov, S. B. Orlinski, and J. Schmidt, *Mater. Sci. Forum* **527–529**, 535 (2006).
- [46] N. T. Son, P. Carlsson, J. ul Hassan, B. Magnusson, and E. Janzén, *Phys. Rev. B* **75**, 155204 (2007).
- [47] N. T. Son, B. Magnusson, and E. Janzén, *Appl. Phys. Lett.* **81**, 3945 (2002).
- [48] M. V. B. Pinheiro, E. Rauls, U. Gerstmann, S. Greulich-Weber, H. Overhof, and J.-M. Spaeth, *Phys. Rev. B* **70**, 245204 (2004).
- [49] B. Magnusson and E. Janzén, *Mater. Sci. Forum* **483–485**, 341 (2005).
- [50] L. Torpo, S. Pöykkö, and R. M. Nieminen, *Phys. Rev. B* **57**, 6243 (1998).
- [51] A. Gali, P. Deák, P. Ordejón, N. T. Son, E. Janzén, and W. J. Choyke, *Phys. Rev. B* **68**, 125201 (2003).
- [52] M. Bockstedte, A. Mattausch, and P. Pankratov, *Phys. Rev. B* **68**, 205201 (2003).
- [53] T. Umeda, N. T. Son, J. Isoya, E. Janzén, T. Ohshima, N. Morishita, H. Itoh, A. Gali, and M. Bockstedte, *Phys. Rev. Lett.* **96**, 145501 (2006).
- [54] P. G. Baranov, I. V. Ilyin, A. A. Soltamova, and E. N. Mokhov, *Phys. Rev. B* **77**, 085120 (2008).
- [55] T. Umeda, J. Isoya, T. Ohshima, N. Morishita, H. Itoh, and A. Gali, *Phys. Rev. B* **75**, 245202 (2007).
- [56] U. Gerstmann, E. Rauls, and H. Overhof, *Phys. Rev. B* **70**, 201204(R) (2004).
- [57] J. Dabrowski and M. Scheffler, *Phys. Rev. Lett.* **60**, 2183 (1988).
- [58] D. J. Chadi and K. J. Chang, *Phys. Rev. Lett.* **60**, 2187 (1988), and references therein.
- [59] E. Rauls, Th. Frauenheim, A. Gali, and P. Deák, *Phys. Rev. B* **68**, 155208 (2003).
- [60] G. A. Baraff and M. Schlüter, *Phys. Rev. Lett.* **55**, 2340 (1985).
- [61] H. Overhof and J.-M. Spaeth, *Phys. Rev. B* **72**, 115205 (2005).
- [62] D. J. Chadi, *Appl. Phys. Lett.* **71**, 2970 (1997).
- [63] N. T. Son, B. Magnusson, Z. Zolnai, A. Ellison, and E. Janzén, *Mater. Sci. Forum* **457–460**, 437 (2004).
- [64] T. Umeda, N. T. Son, J. Isoya, N. Morishita, T. Ohshima, H. Itoh, and E. Janzen, *Mater. Sci. Forum* **527–529**, 543 (2006).
- [65] A. Kawasuso, T. Chiba, and T. Higuchi, *Phys. Rev. B* **71**, 193204 (2005).